Understanding the Influence of Copper on the Color of Glasses and Glazes: Copper Environment and Redox

Laurent Cormier, Cécile Noirot

To cite this version:

Laurent Cormier, Cécile Noirot. Understanding the Influence of Copper on the Color of Glasses and Glazes: Copper Environment and Redox. Glass Europe, 2024, 2, pp.55-82. 10.52825/glass-europe.v2i.1274 . hal-04751501

HAL Id: hal-04751501
https://hal.science/hal-04751501v1

Submitted on 24 Oct 2024

Glass Europe Vol. 2 (2024) 55-81

https://doi.org/10.52825/glass-europe.v2i.1274

Submitted: 12 Apr. 2024 | Accepted:05 Aug 2024 | Published: 23 Aug. 2024

Understanding the Influence of Copper on the Color of Glasses and Glazes: Copper Environment and Redox

Laurent Cormier[1]* and Cécile Noirot[1]

[1]Sorbonne Université, Muséum National d'Histoire Naturelle, UMR CNRS 7590, IRD, Institut de Minéralogie, de Physique des Matériaux et de Cosmochimie, IMPMC, 75005 Paris, France

*Correspondence: Laurent Cormier, laurent.cormier@sorbonne-universite.fr

Abstract. This study explores the influence of copper on the color properties of lead and aluminosilicate glasses by using optical and electron paramagnetic resonance (EPR) spectroscopies. Optical absorption spectra unveil distinct UV absorption characteristics in blue and green compounds, attributed to Cu^+ ions, with notable variations depending on glass composition. EPR quantification of copper oxidation states reveals correlations with color variations, particularly evident in UV absorption shifts towards green colors at lower Cu^{2+} ratios. Redox analysis elucidates color differences in identical compositions subjected to different melting temperatures. Additionally, XANES spectroscopy highlights the role of copper proportions in modulating redox balance. Cu^{2+} site distortions, assessed through Gaussian fitting of optical absorption spectra and EPR simulations, present challenges in determining the impact of site geometry on color. The presence of copper clusters, inferred from broad absorption bands possibly due to Cu^{2+}-Cu^+ intervalence charge transfer (IVCT), suggests their contribution to coloration. The apparition of this IVCT contribution appears as the main reason for the sift in coloration from blue to green as the CuO content increases. Overall, the study emphasizes the multifaceted relationships between copper redox state, site distortions, and clustering phenomena in influencing color perceptions in silicate glasses.

Keywords: Copper, Glass, Glaze, Color, Optical Absorption, XANES, EPR

1. Introduction

The coloration of glasses and glazes has long been a subject of scientific investigation and copper acts as an important chromophore in such materials to achieve specific colors [1], [2], [3], [4], [5], [6], [7]. The historical use of copper dates back to Bronze age, where it was utilized to produce a diverse range of blue earthenware artifacts and glass objects [8], [9], [10]. The introduction of copper imparts the ability to create vibrant blue and green hues, as well as rich red and orange tones [11], [12], [13]. Gaining insight into the mechanisms governing glass coloration and elucidating the influence of factors such as glass compositions or thermal processes is essential for attaining precise control over the final coloration outcomes.

The influence of copper on color is attributed to its ability to exhibit multiple oxidation states, specifically cuprous (Cu^+) and cupric (Cu^{2+}) ions [7], [14]. The color is attributed to the presence of Cu^{2+} ions, while the impact of Cu^+ is generally considered negligible in the visible domain. However, variations in the band due to Cu^{2+} do not always provide a comprehensive explanation for the observed diversity in coloration, particularly in the case of blue and green colors [1], [15]. An example of diverse hues spanning from sky blue to dark-green is displayed in Figure 1 for glazes used at the Manufacture of Sèvres, achieved through the application of

Cu-based pigments. Since the 18th century, the French Manufacture of Sèvres, renowned for its craftmanship in producing fine porcelain artifacts, has been developing various pigments across a broad spectrum of colors. These pigments, when combined with a glass fritt, form the fundamental components of the glaze used for porcelain decorations.

The palette of colors achievable with copper is somewhat more limited compared to pigments based on chromium [16], [17]. Nevertheless, the Manufacture of Sèvres has developed several historical copper-based pigments that are still in used for producing glazes, as detailed in Table S1[1], based on the inventory compiled by d'Albis [18]. Among these pigments, a few compositions contain only copper as a transition element and the glazes depicted in Figure 1 correspond to such pigments. The complex influence of copper redox states and the resulting variations in color remains poorly understood.

The primary objective of this study is to highlight the mechanisms that underlies the different colors observed in glazes and glasses by understanding the role of copper present in Cu^+ and Cu^{2+} ionic forms. This study also assesses the impact of the total copper concentration on its own redox state. To achieve this, the oxidation state of copper is determined using electron paramagnetic resonance (EPR) spectroscopy and X-ray absorption spectroscopy. Additionally, the influence of these interactions on coloration is evaluated through optical absorption spectroscopy.

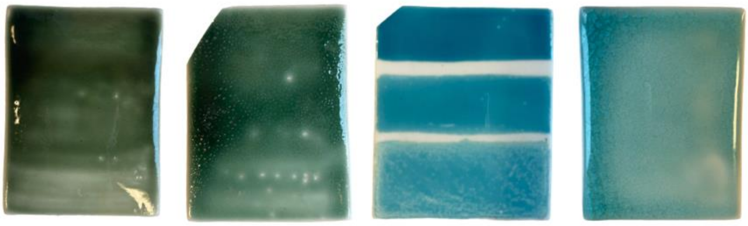

Figure 1. *Ceramic shards glazed with copper glazes of different compositions. The names used at the Sèvres factory are (from left to right): CCPN-16 (dark green), CCPN-17 (water green), EPT-27ter (turquoise) and BX9 (turquoise).*

2. Coloration of glasses containing Cu^{2+} and Cu^+

The oxidation state, the number of neighbors, and the geometry adopted around the coloring element are crucial factors for understanding the origin of color. Copper typically manifests two oxidation states in glasses, Cu^{2+} and Cu^+, both of which coexist, although Cu^+ state tends to predominate [6]. In its the metallic form, Cu^0, copper atoms will precipitate, leading to the formation of nanocrystals.

2.1 Structural environment for Cu^{2+} and Cu^+ ions

In glasses, the structural environment of the two cations, Cu^+ and Cu^{2+}, diverge significantly. Cu^{2+} adopts a configuration surrounded by six oxygen atoms, forming a distorted octahedron [1], [6], [7], [19], [20], [21]. In some isolated studies, CuO_4 sites have been proposed [22], and five-fold coordinated is not excluded [21]. According to EXAFS (Extended X-ray Absorption Fine Structure) studies [21], the Cu-O distances in the octahedral arrangement range between 1.89 and 1.91 Å for the four closest oxygen atoms, with two more distant oxygen atoms between 2.20 and 2.24 Å.

In contrast, the site occupied by Cu^+ is determined by EXAFS as a linearly two-coordinated symmetry, O-Cu-O [6], [21], [22], [23], [24], similar to the Cu environment in cuprite, Cu_2O.

---

[1] Supplementary materials are available at: https://doi.org/10.5281/zenodo.13165792.

However, alternate configurations have been proposed, such as a distorted octahedron or cubic site for Cu-doped silica glass [25] or tetrahedral sites for Cu^+/Na^+ ion exchange glasses [26]. In glasses exclusively containing Cu^+ as the oxidation state, prepared through ionic exchange with Na^+, a notable transition in the coordination environment of Cu^+ was suggested [26]. Specifically, for the most concentrated copper glasses, the coordination number of Cu^+ shifts from 2 to 4, with Cu-O distances extending up to 1.91 Å. These studies suggest a centrosymmetric site for Cu^+, where the O-Cu^+-O angle is constrained to 180°.

Lastly, it has been proposed that both ions reside in distorted octahedral sites [27]. Cu^+ is localized in a compressed octahedron with two-short covalent Cu-O bonds and potentially four longer ionic bonds, although these latter bonds are not experimentally determined by EXAFS. Cu^{2+} is present in elongated octahedra with two long axial and four short in-plane Cu-O bonds.

In copper-doped glasses, the coexistence of the two types of ions is common. The distinctive contributions of each ion to color properties can be elucidated within the framework of the crystal field theory for Cu^{2+} [28], while electronic transitions in the ultraviolet (UV) range account for the coloration induced by Cu^+.

2.2 Origins of color due to Cu^{2+} ions – Jahn Teller effect

The electronic configuration of the Cu^{2+} copper ion is $[Ar]3d^94s^0$. In its crystal field, the electronic configuration is $(t_{2g})^6(e_g)^3$, indicating the presence of a hole in the electron orbitals e_g. An electronic transition $^2E_g \rightarrow {}^2T_g$ is possible without spin reversal (Figure S1). This transition involves the absorption of a photon and is termed a *d-d* transition. Although this transition is spin-allowed, it is prohibited by the Laporte symmetry rule ($\Delta l = \pm 1$).

In the $3d^94s^0$ configuration, the orbitals are asymmetrically populated due to an odd number of electrons in the degenerate e_g orbitals. This introduces instability and an energy gain can be achieved through the emergence of degeneracy in the e_g level. A deformation of the octahedron has precisely this effect and is known as the Jahn-Teller deformation. The axial elongation, schematized in Figure S2, allows, for example, the reduction of interaction between oxygens and the d_{z^2} orbital. This elongation, called tetragonal deformation, is energetically more favorable and the most common deformation for octahedral environments, although some minerals may exhibit copper sites with axial compression. The energy diagram obtained, dependent on the degree of distortion T, is plotted in Figure S1. If the elongation is taken to the extreme, a square planar geometry is obtained, with the energy levels of d_{z^2} and d_{xy} inverted. In an optical absorption spectrum, a tetragonal elongation results in the broadening of the absorption band, which becomes the sum of three gaussians, and can therefore present asymmetries. Three possible transitions exist: d_{xz}or $d_{yz} \rightarrow d_{x^2-y^2}$, $d_{xy} \rightarrow d_{x^2-y^2}$ and $d_{z^2} \rightarrow d_{x^2-y^2}$ [1]. The first transition is more likely since its starting level is degenerated. The absorption it provides will be twice as intense as the other two transitions.

The deformation of the octahedron allows electronic transitions of relatively low absorption intensities. Several studies [1], [20], [29], [30], [31] have determined a molar absorption coefficient for Cu^{2+}, $\varepsilon_{max}(Cu^{2+})$, spanning between 20-75 $L.mol^{-1}$ cm^{-1} (Table 1). In the case of dispersed Cu^{2+} ions within a glassy network, the absorbed photon energy falls within the visible wavelength range, specifically in the region spanning from 10,000 cm^{-1} to 15,000 cm^{-1}. This absorption results in the perception of the complementary color, which ranges from blue to green-blue.

As the concentration of alkali increases or as the alkali size decreases, the tetragonal distortion becomes more pronounced, resulting in a shift in the Cu^{2+} band around 12,500 cm^{-1} to lower energies (higher wavelengths) [19], [20], [21], [29], [32]. A more pronounced elongation of the octahedron increases ligand field strength, shifting the absorption band to higher wavelengths. The degree of Jahn-Teller distortion is characterized by the Cu-O_{eq}/Cu-O_{ax} ratio, representing the ratio between shorter equatorial and longer axial bond lengths (a value of one indicates no distortion) [21]. This ratio varies slightly between 0.84 and 0.86, as the glass composition changes. Another measure of Jahn-Teller distortion is obtained through the energy difference, T, between $d_{z^2} \rightarrow d_{x^2-y^2}$ and $d_{xy} \rightarrow d_{x^2-y^2}$ electronic transitions [1], [21], with T increasing from zero for a regular octahedron to 1.66 for a square planar geometry. The T ratio of these transitions in glasses ranges from 0.72 to .074 [1].

2.3 Origins of color due to Cu^+ ions

In the case of the Cu^+ cuprous ion with the electronic configuration $[Ar]3d^{10}4s^0$, the *d* orbitals are fully filled, rendering *d-d* transitions impossible. Consequently, its presence does not impart visible coloration. Nevertheless, various absorption phenomena may occur, leading to absorption bands in the UV region. These UV absorptions results in strong fluorescence in the visible region with high quantum efficiency, giving interesting properties for tunable lasers or photovoltaic cells [33], [34], [35].

Table 1. *Characteristics of absorption phenomena in the visible and UV regions observed for Cu^+ and Cu^{2+} ions.*

Absorption characteristics and band position (cm^{-1})		**Electronic transitions**	**Molar extinction coefficient ($L.\ mol^{-1}.cm^{-1}$)**	**Refs.**
Cu^+	51,300 (195 nm) 46,400 (215 nm)	$3d^{10} \rightarrow 3d^94p^1$ $3d^{10} \rightarrow 3d^94p^1$		[35] [36]
OMCT	43,500 (230 nm)	Cu^{2+}-O^{2-} CT	2440	[35]
Cu^+	41,700 (240 nm)	$3d^{10} \rightarrow 3d^94s^1$	450	[25]
Cu^+	37,000-38,500 (260-270 nm)	$3d^{10} \rightarrow 3d^94s^1$	~200	[25]
Cu^+	33,333-35,700 (280-300 nm)	$3d^{10} \rightarrow 3d^94s^1$	56	[25]
OMCT	27,800 (360 nm)	O-Cu CT		[37]
IVCT	23,500 (425 nm)	Cu^+-Cu^{2+} IVCT		[38]
OMCT	23,260 (430 nm)	Cu-O CT		[37]
Plasmon	18,200-19,230 (520-550 nm)	Plasmon resonance of Cu_n nanoparticles		[37]
IVCT	20,000 (500 nm)	Cu^+-Cu^{2+} IVCT		[39]
Band gap	17,500 (571 nm)	Cu_2O energy band gap		[40]
Cu^{2+}	15,150-15,900 (630-660 nm)	Cu^{2+} in CuO particles		[37]
Cu^{2+}	10,5900-13,500 (740-950 nm)		20-75	[1],[20],[29], [30], [31]
	8,000-8,500	$d_{z^2} \rightarrow d_{x^2-y^2}$		[1]
	10,600-12,000	$d_{xy} \rightarrow d_{x^2-y^2}$		
	12,000-13,250	$d_{xz}, d_{yz} \rightarrow d_{x^2-y^2}$		
Band gap	2420 (4133 nm)	CuO energy band gap		[40]

The tails of these UV absorption bands potentially extend into the visible spectrum, thereby influencing the perceived color. Multiple absorption phenomena are documented in the literature, and these different transitions are summarized in Table 1. Inter-configurational electronic transitions are reported: $3d^{10} \rightarrow 3d^94s^1$, occurring between ~33,333-41,700 cm^{-1} [25], [33], [34], [36], [41], and $3d^{10} \rightarrow 3d^94p^1$, lying rather deep in the UV region between 46,400-51,300 cm^{-1} [33], [35], [36]. The intensity of the $3d^{10} \rightarrow 3d^94s^1$ transition is lower than that of $3d^{10} \rightarrow 3d^94p^1$, primarily due to the Laporte symmetry rule ($\Delta l = \pm 1$), which prohibits the former but not the latter. However, the $3d^{10} \rightarrow 3d^94s^1$ transition is partially allowed due to ion-network interactions [42]. A highly intense absorption peak observed in the UV region is attributed to the authorized transition $3d^{10} \rightarrow 3d^94p^1$ [41]. However, this transition is considered too distant from the visible range to significantly impact coloration [25], [41]. Oxygen-metal charge transfer (OMCT) between copper and oxygen, or metal-metal intervalence charge transfer (IVCT) between copper ions, can also absorb in the UV range [36], [37], [38], [39]. OMCT often explains the intense UV absorptions of glasses that contain transition metals, even in trace amounts. Indeed, very low concentrations are sufficient since this absorption, allowed by spin and the Laporte rule, is very intense. For copper, these charge transfers lie between 23,000 and 28,000 cm^{-1} [37], or between 23,8000 and 31,250 cm^{-1} [36]. IVCT is possible due to the close proximity of ions with distinct valences, particularly in cases where polyhedra formed by oxygens surrounding copper share an edge, which usually implies clustering of copper ions within the glass. The non-linear trend observed in the optical density with the Cu content has been explained by the occurrence of Cu^+-Cu^{2+} IVCT [43]. The absorption intensity, occurring around 23,500 cm^{-1} [38], [39], is not proportional to the concentration of each species, but rather to the amount of Cu^+-Cu^{2+} pairs [28]. IVCT absorption bands are significantly broader and one to three times more intense than the corresponding *d-d* transitions [28]. An increase in temperature correlates with a decrease in intensity, a characteristic often used for diagnosing the presence of IVCT [44]. However, Mattson and Rossman caution against relying solely on temperature-induced intensity changes as a conclusive indicator of IVCT [45]. They highlight that such a method is primarily based on empirical observations for Fe^{2+}-Fe^{3+} IVCT and may not be universally applicable to other IVCT scenarios. Instead, they propose that the most reliable feature for confirming the presence of IVCT lies in the notably broad width of the absorption bands associated with this charge transfer phenomenon.

To summarize, due to the respective widths of these various UV bands, it can be considered that, optical absorption spectra between 20,000 and 26,000 cm^{-1} are dominated by Cu^+ absorptions [7]. Therefore, an increase absorption near the UV range is presumed to indicate a higher concentration of Cu^+ ions, overlapping with the UV cut-off intrinsic to the glass (band gap).

2.4 Influence of the Cu^+/Cu^{2+} redox state

The pivotal role of the UV region in imparting a blue or green tint to the glass has been previously discussed [1], [15] and discussed in relation to the copper redox state [27], [46], [47], [48], [49]. For instance, a study on calcium-phosphate glasses demonstrated a shift of the UV band towards smaller energies with an increase in Cu^+ concentration [48]. This observed energy shift is found to be directly proportional to the average distance between Cu^+ ions.

The equilibrium between Cu^+ and Cu^{2+} is influenced by factors such as glass compositions and melting temperatures. A higher concentration of Cu^+ is promoted by an increase in alkali proportion [15], [49], [50], larger alkali radii [47], or an increase in the proportion of Al_2O_3 [27]. An anomalous compositional trend for copper in alkali silicate melts, distinct from other multivalent elements, is evident with an increase in Cu^+ content as melt basicity increases, i.e. with an increasing alkali concentration [49]. This phenomenon is explained by the absence of coordination change with the change in the redox state [49]. Alternatively, it has been proposed that a decrease in the coordination number of copper occurs during the reduction of Cu^{2+} to Cu^+ [51], leading to insufficient electron donation to the copper ion for the required reduction in charge. In borate glasses, the behavior differs somewhat, with a maximum in Cu^{2+} content near 18 mol% of alkali oxide due to the borate anomaly [47]. The Gibbs free energy for the $Cu^{2+} \rightarrow Cu^{+}$ reduction reaction increases with temperature for oxides, leading to an expected shift towards Cu^{+} as the melting temperature increases, as observed in various glass systems [46], [52]. The relationship between the redox state and Cu concentration is less straightforward. According to Cable and Xian [46], the Cu^{+}-Cu^{2+} equilibrium is unaffected by the total proportion of CuO, while Durán and Valle [47] suggest that the reduced state is favored by an increase in the total copper concentration. In calcium-phosphate glasses [48], a shift of the UV band towards smaller energies was observed with an increase in Cu^{+} concentration, directly proportional to the average distance between Cu^{+} ions.

While the equilibrium between Cu^{+} and Cu^{2+} is crucial for color formation, studies also highlight the influence of glass compositions on the Cu^{2+} band, leading to a shift in this band that induces color variations [53]. This shift was attributed to varying intensities of the crystal field for Cu^{2+}, dependent on the nature of the added alkali, ranging from 11,600 cm^{-1} to 16,500 cm^{-1}. Additionally, a displacement of the Cu^{2+} band is noted concerning the vitreous matrix: it peaks at 11,000 cm^{-1} for phosphate glasses [1], at 12,700 cm^{-1} for silicate glasses [53], and at 13,800 cm^{-1} for lead borate glasses [31].

Therefore, blue-green color variations can be attributed to (1) changes in the intensity of the crystal field due to compositional effects, (2) changes in the site deformations via the Jahn-Teller effect, deforming the band around 12,500 cm^{-1}, or (3) variations in the UV band due to changes in the redox state. The objective of this study is to discern, for the glass compositions corresponding to the glazes employed at the Manufacture of Sèvres, which of these phenomena contribute to the color variations evident in Figure 1.

3. Samples

3.1 Blue and green glazes: compositions from the Sèvres palette

The studied compositions include the blue and green copper colorations synthesized at the Manufacture of Sèvres, known as CCPN-16 (dark green), CCPN-17 (water green), EPT-27ter (turquoise blue) and BX9. The nomenclature used derives from the standard terminology of the Manufacture. CCPN stands for "Colored Cover for New Paste" (Couverte Colorée de Pâte Nouvelle) and EPT designates "Enamel of Soft Paste" (Email de Pâte Tendre). These designations relate to the type of ceramic that the glass is intended to cover and, more specifically, the type of firing it will undergo. The chosen pigments include the two main glaze color categories: high-fire colors for CCPNs, corresponding to firing temperature above 1100 °C, and low-fire colors for EPT, corresponding to firing temperature between 800-900°C [54]. The BX9 sample, whose name is based on its boron content, is used to obtain a final red color when fired under reduced atmosphere. While all glasses are silicate-based, their compositions vary; BX9 contains boron, EPT-27ter is a lead compound, and CCPNs are aluminosilicates. The proportions of alkalis and copper doping also vary.

The preparation of the coloring powders is achieved at the Manufacture of Sèvres by griding raw materials, as detailed in d'Albis's book [18] and in Table S2. Figure 1 shows ceramic shards covered with these glazes. Both the initial powders and the glaze applied on the ceramic shards are characterized in the supplementary data.

Table 2. *Nominal compositions and compositions measured by EPMA in mol% for the BX9, CCP-16 and CCPN-17 glasses/glazes. Standard deviations are in parenthesis.*

Sample	B_2O_3	Na_2O	MgO	Al_2O_3	SiO_2	K_2O	CaO	TiO_2	FeO	CuO	ZnO	SnO	BaO	PbO
BX9 nominal	8.82	9.17	0.063	2.98	69.12	0.62	0.53	0.008	0.03	0.86	3.76	0.44	3.61	0
BX9 measured	5.2*	8.8(1)	0.02(1)	3.64(1)	66.99(4)	0.43(3)	1.0(2)	nd	0.04(4)	0.57(1)	12.92(7)	0.39(5)	nd	nd
CCPN-16 nominal	-	2.68	0.04	10.53	71.51	2.33	9.28	0.03	0.07	3.54	-	-	-	-
CCPN-16 measured	-	2.64(9)	0.08(6)	9.35(5)	71.8(3)	2.77(3)	9.6(1)	0.001(8)	0.11(3)	3.50(7)	nd	nd	0.019(2)	nd
CCPN-17 nominal	-	2.65	0.04	9.98	72.04	2.34	11.09	0.03	0.07	1.78	-	-	-	-
CCPN-17 measured	-	2.6(1)	0.08(6)	9.1(3)	72.0(1)	2.72(8)	11.3(7)	0.002(9)	0.10(9)	1.82(7)	nd	nd	0.015(3)	nd
EPT-27ter nominal	-	19.34	-	-	48.89	-	-	-	-	6.80	-	-	-	24.98
EPT-27ter measured	-	9.9(1)	nd	0.1(7)	71.5(5)	0.2(3)	nd	nd	nd	6.5(3)	nd	nd	0.02(1)	11.7(4)

nd: not detected

* determined by subtraction

Table 3. *Compositions of the SiAlCu$_x$ glass series measured by EPMA in mol%. Standard deviations are in parenthesis.*

Samples		Na_2O	Al_2O_3	SiO_2	K_2O	CaO	FeO	CuO
SiAlCu$_x$ series	SiAlCu$_{0.5}$	2.6(8)	14.8(1)	68.0(2)	3.97(9)	10.0(1)	0.04(3)	0.5(3)
	SiAlCu$_{0.8}$	2.6(1)	14.8(1)	67.7(2)	3.96(6)	10.1(1)	0.04(3)	0.8(5)
	SiAlCu$_{2.3}$	2.6(7)	14.7(2)	66.7(4)	3.91(9)	9.8(2)	0.04(4)	2.3(9)
	SiAlCu$_{3.6}$	2.5(9-)	14.6(1)	65.8(4)	3.79(9)	9.7(8)	0.04(3)	3.6(5)
	SiAlCu$_6$	2.5(7)	14.2(2)	642(6)	3.71(9)	9.3(9)	0.04(6)	6.0(1)

As the small thickness of the glazes limits their experimental characterization, all pigment mixtures in this study are investigated in the form of bulk glasses, obtained by melting the pigment mixture in a platinum crucible without ceramic support. CCPNs and BX9 glasses are melted at 1280 °C, while the EPT-27ter is obtained at 880 °C, the temperature used for the glaze preparation at Sèvres. To facilitate comparison with other glasses, an additional EPT-27ter glass was also synthesized by melting at 1250 °C. The glasses are shown in Figure 2, revealing that the color variation observed in the glazes is preserved in the glasses. Notably, EPT-27ter and BX9 exhibit a distinct blue color compared to the green CCPN aluminosilicate glasses. Moreover, the EPT-27ter glass melted at 1250 °C has a more pronounced greenish coloration compared to the EPT-27ter glass melted at 880 °C. The compositions for the glazes and the glasses are identical and summarized in Table 2.

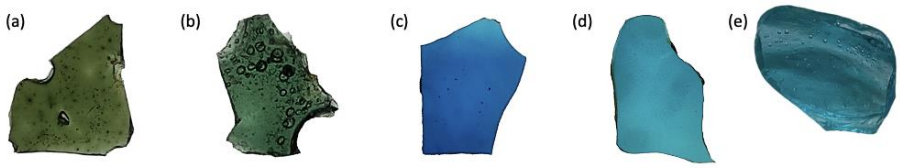

Figure 2. *Glasses prepared from the pigments used at the Manufacture of Sèvres: (a) CCPN-16 'dark green', (b) CCPN-17 'water green', (c) EPT-27ter-880°C 'turquoise', (d) EPT-27ter-1250°C and (e) BX9.*

3.2 SiAlCu$_x$ glass series

The SiAlCu$_x$ series explores variations in the proportion of copper alone (x = 0.5-6 mol%). It closely resembles CCPN-16 and CCPN-17 from the blue/green palette of glazes used at Sèvres. Glasses are prepared from dried reagent grade powder oxides and cabonates that were homogenized through manual grinding in an agate mortar with ethanol. An initial decarbonatation step was performed at 850 °C for one night, and the desorbed CO_2 mass was monitored through weighting. The mixture was then melted in an electric furnace at 1380 °C followed by quenching. A melting time of 4 hours is used to eliminate bubbles, which still persist in the least concentrated copper samples. These compositions are detailed in Table 3. The SiAlCu$_x$ glasses exhibit color variations based on the copper content. For instance, CCPN-16 and CCPN-17, differing only in their copper contents, produce "dark green" and "water green" colors, respectively (Figure 3).

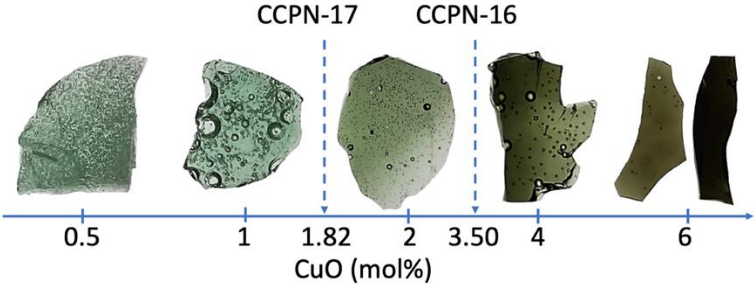

Figure 3. *Picture of the glasses of the SiAlCu$_x$ series as a function of the CuO mol% and the CCPN-16 and CCP-17 glazes used at the Manufacture of Sèvres. The last picture shows the most concentrated glass with two thicknesses (330 µm and 1 mm) to highlight the color and the reduced transparency of the highly concentrated glasses.*

4. Experimental methods

4.1 Electron Probe Micro-Analysis (EPMA)

The elemental analysis of the glass samples was carried out on the CAMPARIS electronic micro-probe platform (Sorbonne University, Paris) using a Cameca SX-Five (Ametek-Cameca, France). The glasses, embedded in resin, were polished to a particle size of 1 µm. An electron beam, generated by a tungsten filament, was focused on a micro-metric area of the sample, enabling the removal of core electrons from the atoms of the material. The emitted X-rays, upon returning to the ground state, are characteristic of the present elements. These emission lines were analyzed using wavelength dispersion spectrometers, calibrated with known minerals containing the elements to be detected. However, light elements, such as oxygen and boron, pose challenges and were not analyzed. Boron concentration is derived by subtracting the total detected oxide percentage from 100 %. The oxidation state is also not determined. To assess the average glass composition and verify its homogeneity, ten distinct points are measured. The average and the standard deviation are calculated and reported in Table 2 and Table 3.

4.2 Differential Scanning Calorimetry (DSC)

The glass transition temperatures were determined using Differential Scanning Calorimetry (DSC). The glass is first crushed and sieved to retain only particles with a size of 50-100 µm. Approximately 70 mg of sample is placed in a platinum crucible. The measurements are carried out using a LABSYS-evo SETARAM instrument, with a heating treatment up to 1000 °C at a rate of 10 $°C.min^{-1}$ under a constant flow of argon.

4.3 Optical absorption spectroscopy

The optical absorption spectra are recorded using a PerkinElmer Lambda 1050 spectrometer, which covers a wide range from ultraviolet (UV) to near-infrared (NIR). To cover this extensive spectrum, the spectrometer uses two lamps: a tungsten halogen filament lamp for the visible-NIR range (319.2-3,300 nm) and a deuterium lamp for the UV energy range (200-319.2 nm). Three detectors, each sensitive to different energy domains, are utilized: a photomultiplier (250-860.8 nm), an InGaAs photodiode (860.8-2,500 nm) and a PbS photoconductor (2,500-3,100 nm). A monochromator is used to scan the energy range, modulating the wavelength of the beam during the measurement. When the glass under investigation lacks bubbles, its spectrum can be accurately measured through transmission, which is the preferred method. However, if the presence of bubbles hampers transmission measurements, an integrating sphere has been used as an alternative method.

4.3.1 Glass without bubbles: transmission measurements

Prior to measurement, each glass slide is polished on both sides using silicon carbide sheets and diamond pastes, with the finest grain size used being 1 µm. This polishing ensures that the glass blades have parallel faces, free of scratches. The spectrometer operates by comparing two beams: one passing through the glass blade and the other serving as a reference, following an identical path but without a sample. Absorbance measurement without the glass blade is also recorded to correct the spectrum for potential variations in support alignment or detector sensitivities at different wavelengths. This reference absorbance is subtracted from the optical spectra of the glasses. The transmission, defined as the intensity ratio between the sample beam (I) and the reference beam (I_0) for each wavelength, T = $\frac{I}{I_0}$, is converted to absorbance (A) using the following relationship:

$$A = log_{10}\left(\frac{1}{T}\right) \tag{1}$$

Absorbance is more conveniently related to physical characteristics such as thickness (L) or the concentration of absorbent species (C) through the Beer-Lambert law:

$$A = \epsilon L C \qquad (2).$$

Here, ε represents the molar absorption coefficient ($L.cm^{-1}.mol^{-1}$), which is independent of both L or C. However, for the same absorbent species, ε can vary with the atomic environment of the species, its state of spin or oxidation.

4.3.2 Glasses with bubbles: measurements with the integrating sphere

When the glass contains numerous bubbles, as it is the case with the laboratory-prepared CCPN-17, correct measurements through transmission become challenging due to light diffusion caused by the bubbles. Consequently, the spectra are measured using an integrating sphere. In this setup, the glass is positioned within a hollow sphere with walls exhibiting very low absorption across the studied energy range. The incident beam is directed onto a smooth face of the glass. While the light passes through the glass, it undergoes deflection by the bubbles. The sphere effectively collects the remaining intensity in all directions and the detector measures the absorption of the beam by the glass. To correct for any absorption introduced by the sphere walls, a measurement is obtained with a $BaSO_4$ plate replacing the glass, giving a spectrum that is subtracted from that of the glass. The diffuse reflectance spectra obtained were transformed into a remission function, *F(r)*, through the application of the Kubelka-Munk formula [55]:

$$F(r) = \frac{(1-R^2)}{2R} \qquad (3)$$

where R is the reflectance signal.

4.4 Electronic Paramagnetic Resonance (EPR) Spectroscopy

EPR spectra were acquired using a Bruker ESP300 spectrometer operating in the X-band with parameters reported in Table 4. The (derived) absorption of microwaves at fixed frequency is measured while varying the applied external magnetic field. The glasses are ground into powder using an agate mortar and the powder is then placed into a highly pure silica glass tube, intentionally free of any absorbing center, such as Fe^{3+}. As a reference for calculating the number of spins, an alanine standard is used. The amount of Cu^{2+} species depends on the mass introduced into the EPR tube and the intensity of the EPR bands will be directly related with the quantity of Cu^{2+}.

Table 4. *Parameters used for EPR measurements.*

Microwave power	Modulation amplitude	Microwave frequency	Time constant	Conversion time
1 mW	3 mT	9.86 GHz	327 ms	146 ms

In EPR spectra, the measured quantity is the derivative of the absorbance and the integral value of EPR spectra is directly proportional to the spin content in the sample [56]. The number of Cu^{2+} ions in the samples are determined using the formula:

$$n(Cu^{2+}) = n\left(Cu^{2+}_{std}\right)\frac{G_{std}S}{S_{std}G} \qquad (4)$$

Here, G and G_{std} refer to the detector gains applied to glass and alanine, respectively, while S and S_{std} represent the normalized double integrals measured for the corresponding spectra. The S_{std} value varies slightly for different measurements and this variability is represented in the dosage results through error bars. Measurements were conducted under identical conditions, except for the detector gain. In cases where conditions differ, it becomes necessary to normalize the double integrals by the amplitudes of modulation or the square of the number of scans.

Finally, molar concentrations of Cu^{2+} are calculated as:

$$[Cu^{2+}] = n(Cu^{2+})\frac{M_{glass}}{m} \quad (5)$$

where *m* denotes the mass of glass introduced into the tube, and M_{glass} is the molar masses of the glasses, derived from EPMA-measured compositions. The ratio used is $\frac{[Cu^{2+}]}{[Cu_{tot}]}$, where $[Cu_{tot}]$ represents the total Cu concentration.

4.5 X-ray Absorption Spectroscopy

XANES (X-ray Absorption Near Edge Structure) spectra were collected on two different beamlines at the SOLEIL synchrotron facility (Saint-Aubin, France), operating at 2.72 GeV and 500 mA.

XANES spectra at the Cu K-edge were acquired on the SAMBA beamline, using a Si(220) double crystal monochromator [57]. Data collection was conducted in transmission mode on glass slab or pellets according to the copper content. A beam size of 300 × 300 μm^2 was used with an energy resolution of 0.25 eV. A Cu metallic foil was used for energy calibration, with the first inflection point of the edge set to 8978.9 eV [58]. The edge energy was determined at the position of the first derivative maximum of the main absorption edge, and spectra were normalized using linear pre- and post-edge background functions. All data analysis procedures were conducted using the Athena software [59].

The Cu L_3-edge XANES spectra were acquired on the LUCIA beamline [60], using total fluorescence yield detected by a SDD. A Kohzu five-components double crystal monochromator was used for the incoming X-rays. Spectra were recorded using a beam size of 5x200 μm^2. A resolution of 0.1 eV was fixed, with each step lasting 4 seconds and two spectra were averaged to improve the signal-to-noise ratio. Energy calibration was performed by setting the edge (the derivative of the first maximum) of the XANES spectrum of tenorite CuO to 931.2 eV [61]. For data processing, a linear pre-edge normalization function and a third-order polynomial fit on the post-edge region were applied. The value of the polynomial fit was anchored at the edge step.

5. Results

5.1 EPMA results

The nominal compositions of CCPN-16 and CCPN-17 glazes differ slightly in their main components and significantly in their initial copper oxide concentration, with 3.54 and 1.78 mol% for the CCPN-16 and CCPN-17, respectively (Table 2 and Table S2). This difference in CuO content likely accounts for the variation in color, as CCPN-16 appears darker than CCPN-17 (Figure 1).

Table 2 details the compositions of the blue and green glasses under investigation. The nominal compositions, calculated from the recipes outlined in "Traité de la Porcelaine de

Sèvre" [18], include natural materials like Fontainebleau sand or Finnish pegmatite. The calculation of nominal compositions relies on elementary analyses of these materials conducted at the Manufacture of Sèvres and results were compared with data obtained through EPMA. Discrepancies between calculated and EPMA-measured compositions occasionally reach few percents, reflecting inherent variabilities present in natural raw materials.

In the case of EPT-27ter, there is a notable deficiency in sodium oxide in the measured composition compared to the nominal one (Table 2). Additionally, it is observed that the molar percentage of Na_2O is significantly higher compared to the CCPN glazes.

The copper proportion decreases with the cumulative melting time, as measured by EPMA (Figure S11). Copper tends to partially leave the glass during melting, indicating the diffusion of copper into the platinum crucible containing the glass. This interpretation is supported by an observation during crucible cleaning: the carbonates and borate mixture used for cleaning takes on a relatively sustained green-blue color, indicating the recovery of the diffused copper in platinum.

5.2 Influence of copper on the glass transition temperatures

Glass transition temperatures (Tg) were measured for the $SiAlCu_x$ glasses containing more than 1 mol% CuO (Figure 4). Below 1 mol% CuO, no notable change in Tg is anticipated. However, beyond a few mol%, the structure, particularly the network connectivity, may be affected by the added elements, potentially leading to variations in Tg values. Figure 4 illustrates that the addition of copper results in a decrease in Tg values, suggesting a modifying role for copper within the aluminosilicate network.

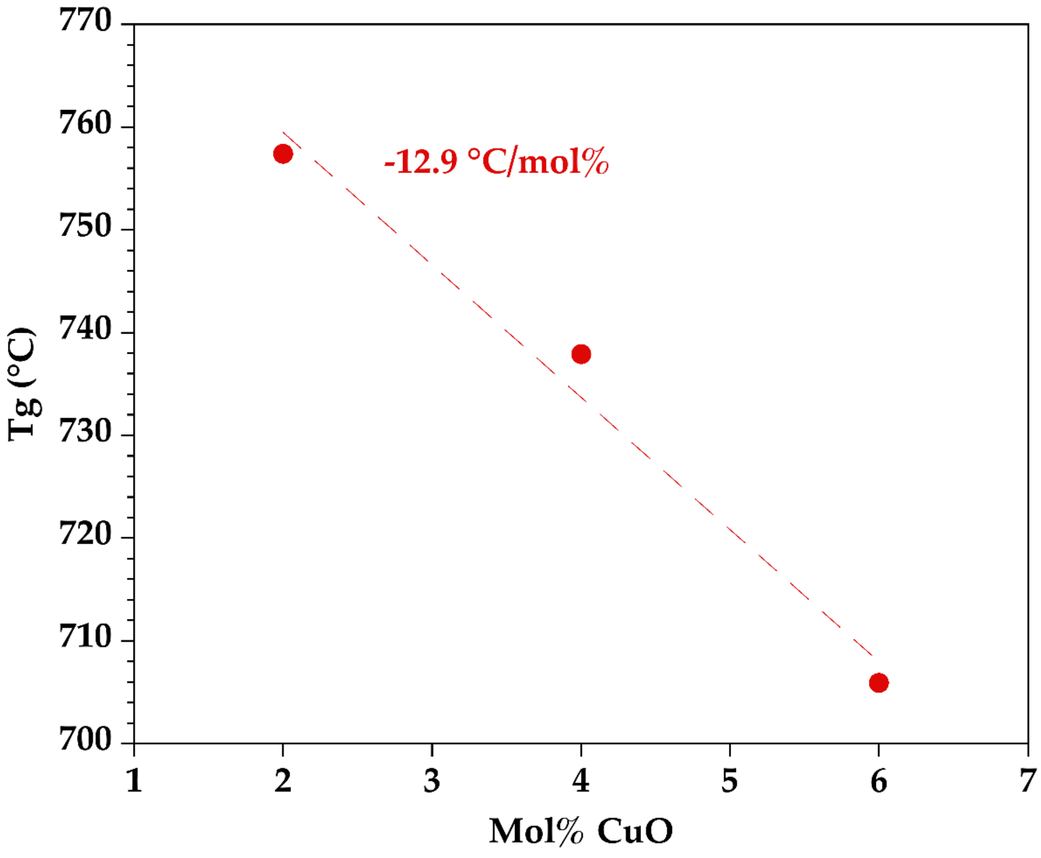

Figure 4. *Impact of Cu on the glass transition temperatures (Tg ± 5 °C). The value indicates the slope of the linear fit represented as a dashed line.*

5.3 Results for the blue and green copper glazes

5.3.1 Optical absorption spectra

The optical absorption spectra for glasses produced by firing glaze compositions from the Manufacture of Sèvres are presented in Figure 5a. The measured absorption is normalized by the thickness of the thin glass slide, revealing different intensities that are associated with the concentration of Cu^{2+} in glass. To facilitate the comparison of the positions and shapes between spectra, Figure 5b normalizes the spectra to the maximum absorption of the Cu^{2+} band. The absorption minimum, within the range 17,500-25,000 cm^{-1}, is a representative indicator of perceived color. A shift towards green color corresponds to lower energies. Figure 6 shows the variations in the positions of the maximum absorption related to Cu^{2+} and the minimum absorption for the different compositions.

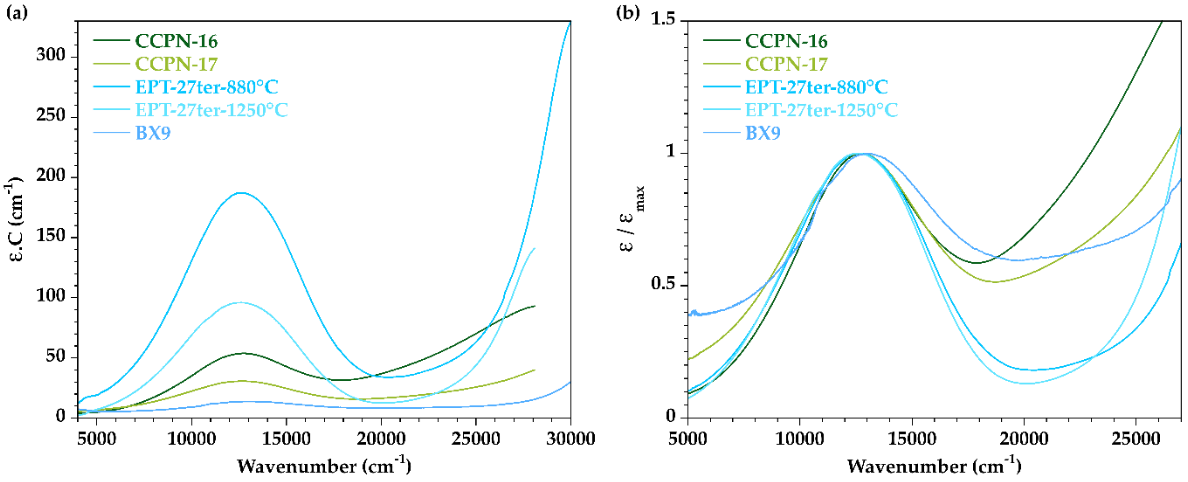

Figure 5. *UV-visible-IR spectra for glazes (a) normalized by the thickness and (b) normalized by the maximum absorption of the band due to Cu^{2+} near 12,600 cm^{-1}.*

In the case of EPT-27ter glasses, there is a significant reduction in intensity as the melting temperature increases. The Cu^{2+} absorption band is centered at 12,642 cm^{-1} for both glasses (Figure 6a) but the minimum absorption is slightly red-shifted for the glass melted at 1250 °C compared to the one melted at 880 °C (Figure 6b). This is consistent with the more pronounced blue-green coloration for EPT-27ter-1250°C (Figure 2). The reduction in intensity of the Cu^{2+} absorption band suggests a lower Cu^{2+} content for the EPT-27ter-1250°C glass, which is expected as Cu^{+} is favored at high melting temperature. This copper redox change affects both the Cu^{2+} band and the UV band, explaining the color variation.

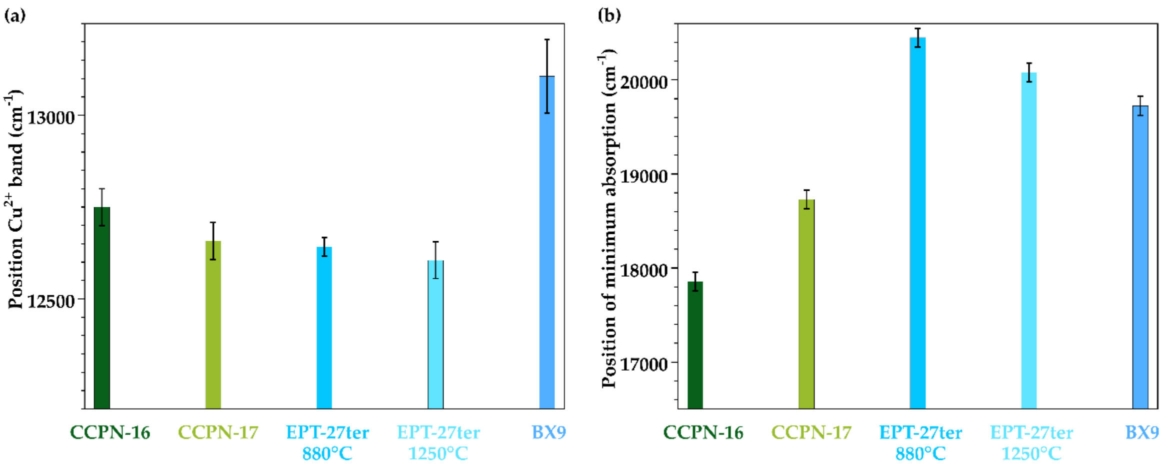

Figure 6. *(a) Position of the Cu^{2+} band. (b) Position of the minimum absorption defining the highest transmission.*

CCPN-16 and CCPN-17 have a minimum absorption at 17,859 cm^{-1} and 18,730 cm^{-1}, respectively. The shift in the minimum absorption results in the 'dark green' coloration for CCPN-16 and 'water green' for CCPN-17. In the chromaticity diagram (Figure S10), CCPNs colors shit from the center of the diagram (before firing) to the 'dark green' and the 'water green' for CCPN-16 and CCPN-17 glazes.

5.3.2 Fit of the Cu^{2+} absorption band

In optical absorption spectra, the Cu^{2+} absorption band, near 12,600 cm^{-1}, has minimal variation. However, even slight changes can provide insight into the geometry of the Cu^{2+} site. The octahedral geometry is expected to be distorted due to axial elongation, as predicted by the Jahn-Teller effect. The absorption band can then be fitted using three Gaussian peaks, each corresponding to an electron transition as per the copper energy diagram in the elongated octahedron (Figure S12). The most energetic peak ($d_{xz}, d_{yz} \rightarrow d_{x^2-y^2}$) is expected to be twice as intense as the other two transitions ($d_{xy} \rightarrow d_{x^2-y^2}$and $d_{z^2} \rightarrow d_{x^2-y^2}$) given the degeneracy of the starting level. The three Gaussians are adjusted to minimize deviations from the experimental spectrum after the removal of a linear baseline. Typical fits are presented in Figure S13, and the centers and full-width at half maximum (FWHM) of the three Gaussian are reported in Table 5.

Table 5. *Gaussian parameters used for the fitting of the Cu^{2+} absorption band. The error for the peak position and full-wdith at half maximum is estimated to be ± 50 cm^{-1}. The degree of tetragonal distortion is $T = \frac{energy(peak3)}{energy(peak2)}$.*

	Peak	CCPN-16	CCPN-17	EPT-27ter 880°C	EPT-27ter 1250°C	BX9
Position (cm^{-1})	3 2 1	10,256 12,208 13,422	9,350 11,378 13,375	8,903 11,271 13,653	9,864 11,389 13,912	9,533 11,906 13,860
FWHM (cm^{-1})	3 2 1	4,234 4,039 4,593	4,537 3,662 4,896	3,975 3,509 5,338	5,291 3,713 4,971	2,884 3,033 4,960
Degree of tetragonal distortion T		0.840	0.822	0.790	0.866	0.801

The degree of distortion (T) can be estimated from the energy differences between the electronic transitions corresponding to peaks 3 and 2 [1]. The T values reported in Table 5 show that the greater the ratio, the higher the site elongation, as the energy gap between the levels d_{z^2} and $d_{x^2-y^2}$ increases, while the gap between d_{xy} and $d_{x^2-y^2}$ varies little or remains constant. The T values are relatively constant within 0.79-0.87 and are higher for the glasses melted at high temperature, suggesting a relationship with the copper redox state. The site distortion increases as the Cu^{2+} content decreases at high melting temperatures.

5.3.3 Determination of the copper redox state using EPR spectroscopy

Electron paramagnetic resonance (EPR) spectroscopy was used to determine the redox ratio between the two oxidation states, Cu^{2+} and Cu^{+}. The intensity of the spectra plotted in Figure 7a provides an indication of the number of Cu^{2+} ions detected. The ratios $\frac{[Cu^{2+}]}{[Cu_{tot}]}$ for the various glasses are calculated from the double integrals of the spectra, following the method described in §4.4. These ratios are presented in Figure 7b.

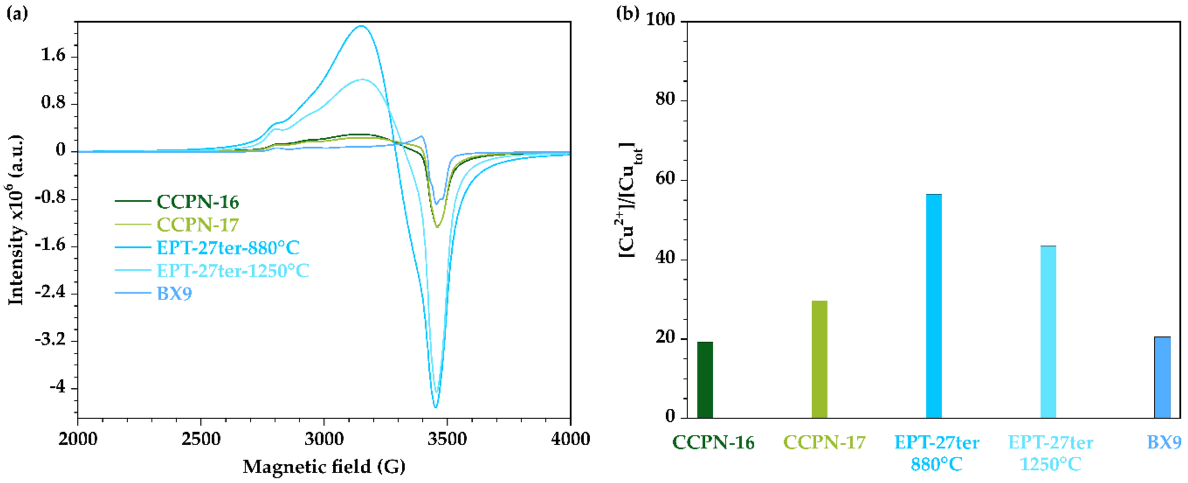

Figure 7. *(a) EPR spectra for the various samples from Sèvres. (b) Copper redox ratio with Cu^{2+} determined by EPR and total copper content measured by EPMA.*

5.3.4 Local copper symmetry measured by EPR

The shapes of the EPR spectra in Figure 7a are indicative of the environments occupied by the absorbing center. In the case of an elongated octahedron, the axial geometry is reflected in the Landé factors (coefficients of the matrices *g*) and hyperfine coupling constants (A), which show identical values along the *x* and y directions but differ from the value along the *z* direction. The *x* and *y* directions, perpendicular to the symmetry axis of the site, are denoted by indices ⊥ , and the *z* direction, parallel to the symmetry axis, is denoted by the index ∥. Axial geometry results in spectra resembling that of the spectrum for BX9 (Figure S14). At low magnetic field (or large *g* values), the hyperfine structure is observed for the *z* direction parallel to the external field in the form of four bands separated by the constant $A_{\parallel}$ ($A(Gauss) = \frac{A(eV)}{g\beta}$, with β the Bohr magneton) and centered on $g_{\parallel}$. The magnetic field H_0 and *g* are related by the resonance condition: $g = \frac{h\nu}{H_0\beta}$, with h the Planck constant and ν the frequency. Only the first three peaks are observed on the spectrum for BX9. The high magnetic field region allows for the extraction of characteristic EPR parameters for the *x* and *y* directions, perpendicular to the main axis. The spectrum, derived from absorbance, changes sign at the field corresponding to $g_{\perp}$. The hyperfine structure is less apparent in this region, making the determination of $A_{\perp}$ approximate. The peak width is influenced by the different orientations and the variations in the values of *g* and A according to the considered sites, expressed as $\delta g_{\parallel}$, $\delta g_{\perp}$, $\delta A_{\parallel}$ and $\delta A_{\perp}$. To evaluate all these parameters, we use the code EasySpin to fit the spectra [62], assuming axial symmetry for BX9. The shape of the BX9 spectrum and the adjustment results (Table 6) confirm the presence of Cu^{2+} in an elongated octahedron with axial symmetry, where $g_{\parallel} > g_{\perp}$ (one would have $g_{\parallel} < g_{\perp}$ for a compressed octahedron).

On the contrary, the other spectra exhibit a different shape than that corresponding to an axial symmetry. Notably, a broad and intense peak appears between 3,000 and 3,250 G, falling between the field values corresponding to those of $g_{\parallel}$ and $g_{\perp}$ for BX9. This difference could stem from a rhombic deformation of the site, indicating less symmetry. In this scenario, the *x* and *y* directions would no longer be equivalent, imposing $g_x \neq g_y \neq g_z$, with $g_x < g_y < g_z$ by convention. An alternative explanation for this broad peak is the potential formation of copper clusters, wherein copper sites share edges [19]. However, simulating such clustering proves challenging and this has not been explored in this study. Instead, we adjust the parameters *g*, A, δg and δA for the three non-equivalent directions using EasySpin, assuming a rhombic deformation. The experimental and simulated spectra are compared in Figure S15 and fitting result are summarized in Table 6. Assessing values for A are challenging when hyperfine structures are not resolved, resulting in significant relative uncertainties for the A and δA along *x* and *y*.

Table 6. *Parameters used to fit the EPR spectra (g without unit, A in Gauss). Error values for g et δg are ± 0.01 (and ± 0.005 when indicated by *). Error values for A et δA are ± 3 Gauss.*

	g_x	δg_x	g_y	δg_y	g_z	δg_z	A_x	δA_x	A_y	δA_y	A_z	δA_z
CCPN-16	2.05	0.021*	2.12	0.21	2.35	0.11	3	3	50	3	125	35
CCPN-17	2.05	0.021*	2.09	0.24	2.35	0.11	3	3	50	3	125	35
EPT-27ter 880°C	2.051*	0.041*	2.138*	0.155*	2.37	0.12	3	3	50	3	125	20
EPT-27ter 1250°C	2.045*	0.074*	2.163*	0.11	2.37	0.12	3	3	50	3	125	10
	$g_{\perp}$	$\delta g_{\perp}$	$g_{\parallel}$	$\delta g_{\parallel}$	$A_{\perp}$		$\delta A_{\perp}$		$A_{\parallel}$		$\delta A_{\parallel}$	
BX9	2.055*	0.05	2.34*	0.09	15		3		132		25	

5.4 Results for $SiAlCu_x$ glass series

The optical absorption spectra for the $SiAlCu_x$ series are shown in Figure 8. Below 2 mol% CuO, the optical absorption spectra exhibit a similar shape with increasing copper concentration, as illustrated by the change from 0.5 mol% to 1 mol% CuO in Figure 8. However, above 2 mol% CuO, there is a notable change with the progressive addition of copper. Compared to the Cu^{2+} absorption band, there is increasing absorption between 18,000-27,000 cm^{-1}, thereby extending into the visible range. This absorption in the blue region significantly modifies the color by red-shifting the minimum absorption.

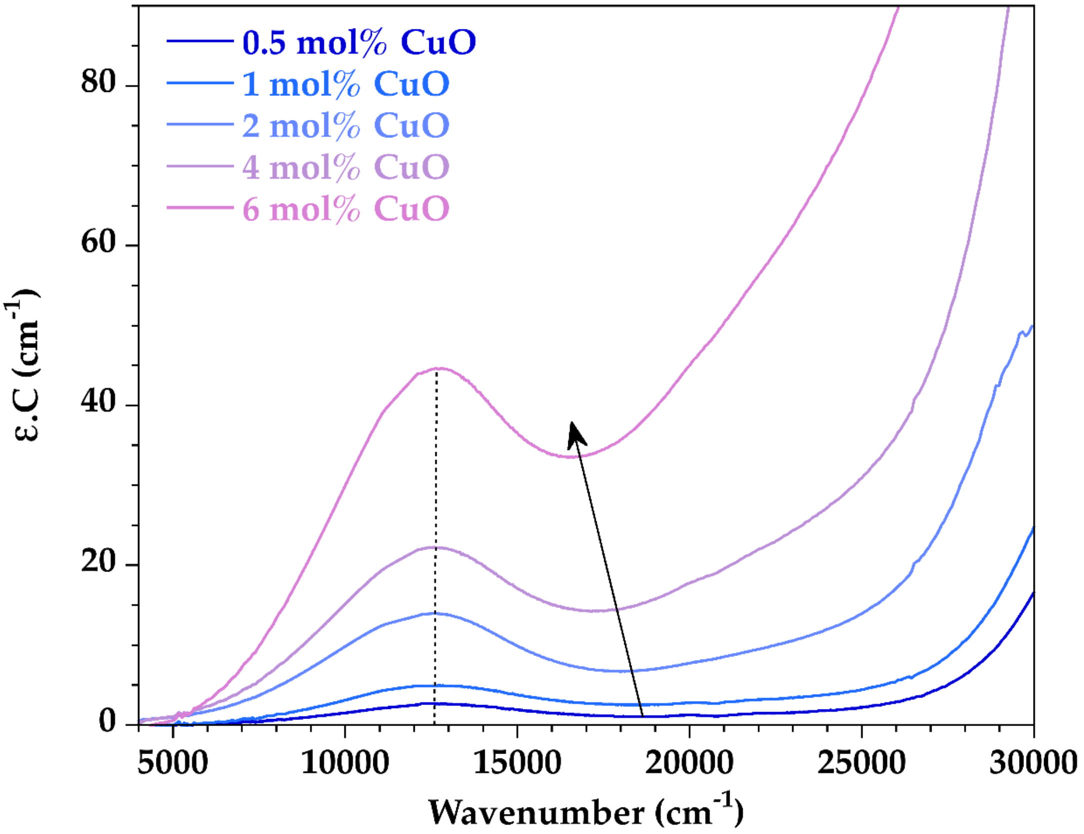

Figure 8. *Optical absorption spectra in transmission for the SiAlCu$_x$ series.*

EPR spectra for the SiAlCu$_x$ series are shown in Figure 9a. With the addition of copper, the spectra lose the resolution of the hyperfine structure, and there is a decrease in the normalized intensity. Figure 9b shows the copper redox ratio $\frac{[Cu^{2+}]}{[Cu_{tot}]}$ derived from these spectra, suggesting that the addition of copper beyond a few mol% results in the reduction of copper.

Similar modifications of the EPR spectra are interpreted as the site deformation, from stretched octahedra (Jahn-Teller distortion) to rhombic symmetry [63], [64]. However, an alternative explanation for this behavior has also been proposed [19], [63], [65], [66], [67], [68], [69], by considering magnetic dipole interactions at high CuO concentrations. Spectra can be effectively considered as the sum of these two contributions [19]. Beyond 15-20 mol% CuO, the prevailing interaction type is a magnetic super-exchange interaction, involving the coupling of spins in antiparallel configuration. Coupled spins are no longer active in EPR, and dipole interactions vary according to $1/r^3$ with r the distance between two ions [70]. This suggests the formation of copper ion clusters, where octahedra share edges or faces without necessarily deforming [67]. The decrease in intensity and the deformation of the EPR spectra can thus be interpreted as indicative of the formation of copper ion clusters. Therefore, EPR spectra likely do not signify a change in the copper redox.

The tendency to form clusters is composition-dependent. Glasses such as borates, phosphate, tellurides and silicates are widely investigated [19], [63], [65], [66], [67], [68], [69], revealing shifts in the concentrations at which these effects manifest in EPR. For instance, the addition of boron can tolerate a higher copper content before observing the EPR deformation, as boron partially hinders cluster formation [67].

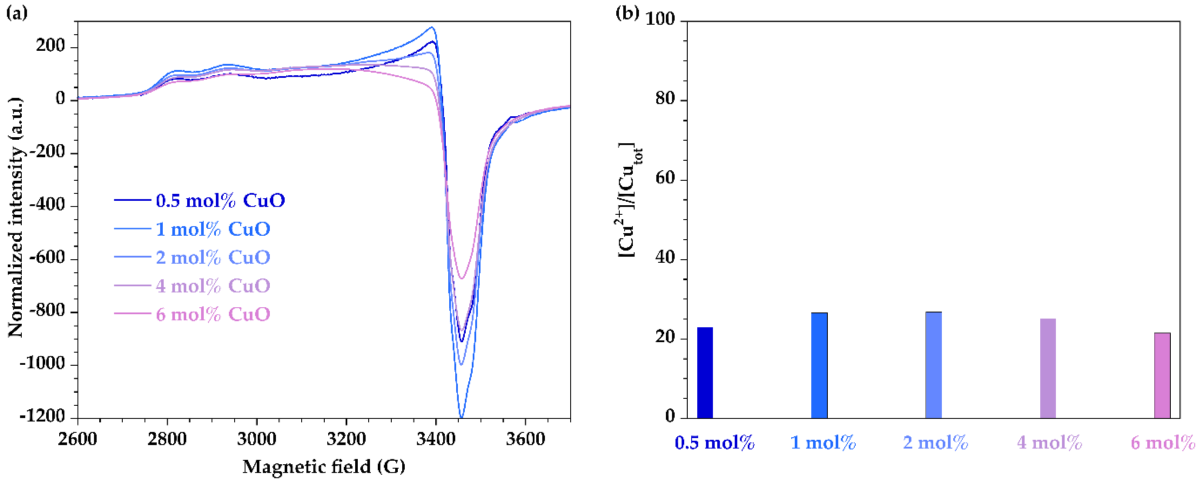

Figure 9. *(a) EPR spectra normalized by the acquisition parameters and by the total Cu concentration determined by EPMA for the SiAlCux series. (b) Copper redox dosage determined by EPR as a function of the copper concentration in the SiAlCux series.*

Given the uncertainties regarding the EPR quantification of the redox state due to potential spin interactions, an alternative technique is used to assess the influence of copper addition on its oxidation state. XANES spectroscopies at the copper L_3-edge (Figure 10a) and K-edge (Figure 10b) are used for this purpose. For the L_3-edge, the peak at 931.6 eV is associated with Cu^{2+} and increases in intensity with the addition of copper. Similarly, for the K-edge, the peak at 8983 eV associated with Cu^{+} decreases with copper addition. Therefore, in contrast with the EPR quantification, XANES spectra reveal that the addition of copper tends to oxidize rather than reduce it.

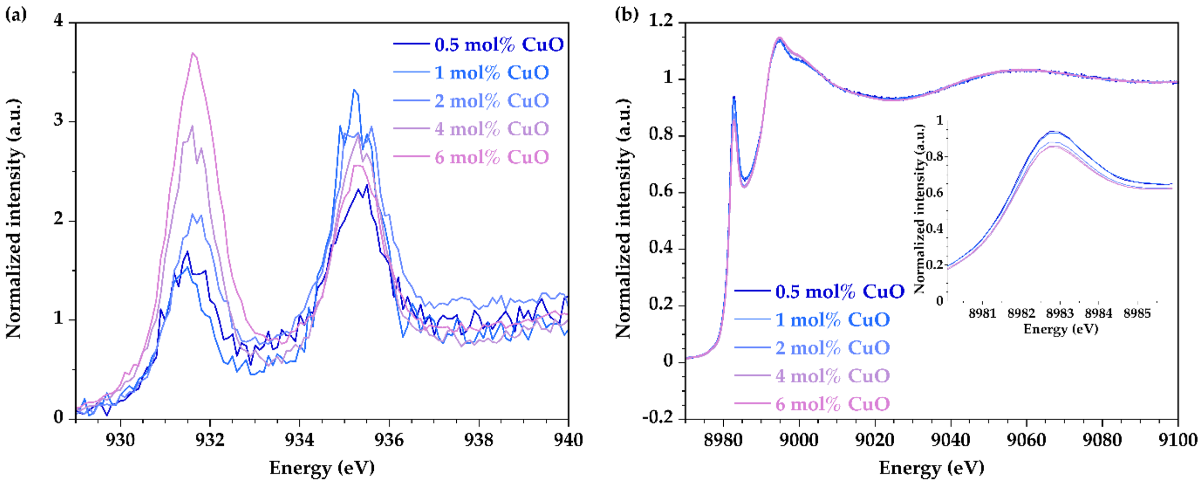

Figure 10. *XANES spectra for the $SiAlCu_x$ series at the (a) L_3-edge and (b) K-edge.*

To compare these results with the EPR quantification of the copper redox ratio (Figure 9b), a redox ratio assessment is obtained from the XANES spectra at the Cu K-edge. For this purpose, a linear combination adjustment of reference spectra is performed using the Athena software between 8960 and 9080 eV. The reference compounds used are azurite $Cu_3(OH)_2(CO_3)_2$ for Cu^{2+} and a reference glass for Cu^{+}, having a known $\frac{[Cu^{2+}]}{[Cu_{tot}]}$ ratio of 0.255 [12]. A typical example of fit is shown in Figure S16. The fit score R, defined as $R=\Sigma(\text{experimental - fit})^2 / \Sigma(\text{experimental})^2$, remains between 0.011 and 0.013, with lower scores indicating better adjustments.

The redox ratios calculated from EPR and XANES are presented in Figure 11. At low copper concentrations, the XANES values align with those from EPR. This validates the linear combination method. However, starting from 2 mol% CuO, the redox estimated by EPR and XANES diverge. The redox ratio measured by XANES remains constant, whereas EPR suggest a reduction of Cu^{2+} ions. Consequently, the XANES analysis provides evidence that the EPR quantification is inaccurate for copper concentrations exceeding ~2 mol% CuO.

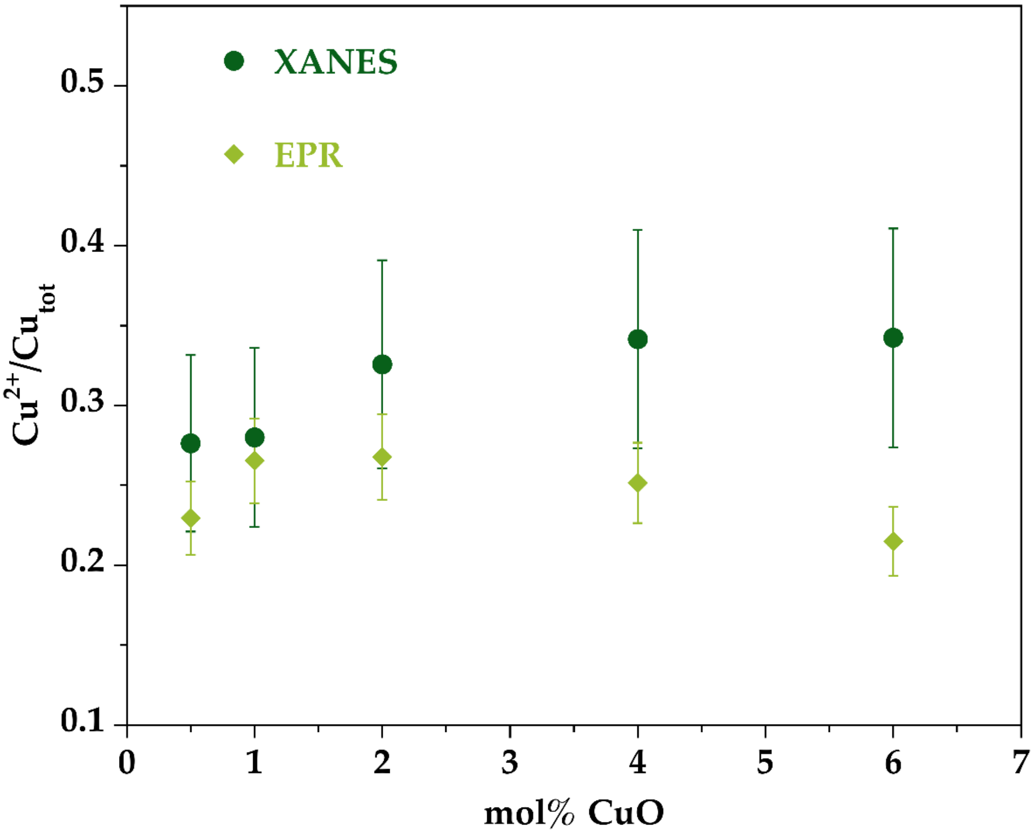

Figure 11. *Comparison between the redox ratios determined by EPR and XANES for the $SiAlCu_x$ glass series.*

5.5 IVCT occurrence? Optical absorption spectroscopy in temperature

As shown in Figure 5 and Figure 8, a notable absorption between 18,000-27,000 cm^{-1} is evident, exerting a pronounced influence on the glass color. This absorption phenomenon induces a red shift in the minimum absorption, resulting in a greener coloration. One plausible explanation for this absorption may be a Cu^{+}-Cu^{2+} IVCT, which is expected to occur in proximity to this energy range (Table 1). In well-characterized cases, such as IVCT involving Fe^{2+}-Fe^{3+} or Fe^{2+}-Ti^{4+}, it is known that the intensity of the IVCT band increases with a decrease in temperature [28], [71]. This temperature dependence has been demonstrated in obsidians, explaining their specific color [44].

In previous studies addressing Cu^{+}-Cu^{2+} IVCT, the potential dependence of IVCT on temperature is never considered. Instead, identification is typically based on energy consideration, when calculations of ion energy levels are feasible, particularly in the case of complexes [38], [72]. Additionally, the significant width of the absorption peak is used as a crucial criterion for identification. In the spectra presented in Figure 8, the suspected absorption attributed to IVCT between 18,000-27,000 cm^{-1} does not exhibit a well-resolved Gaussian contribution, preventing the measurement of peak-width though the shape could be indicative of a very broad contribution.

Figure 12 shows the temperature-dependent variations of optical absorption spectra for the SiAlCu$_x$ series, specifically focusing on the most concentrated copper content. The absorption within the range 18,000-27,000 cm^{-1} remains largely unaffected by changes in temperature. Instead, there is an observable shift of the UV edge beyond ~27,000 cm^{-1} towards higher energies with decreasing temperature. This behavior is consistent with the description provided by Burns regarding OMCTs [28], which contribute to the UV absorption edges in our glass compositions. Consequently, temperature measurements do not provide strong evidence for the presence of IVCT. However, this does not entirely rule out the hypothesis of such transitions, as temperature measurements are not regarded as a definitive test in the case of Cu^{+}-Cu^{2+} charge transfers [45]. It is worth noting that the temperature dependence of IVCT bands is reliably characterized for specific cations but is not universally expected for all IVCT [45]. Therefore, the most reliable feature of IVCT bands lies in their broad width.

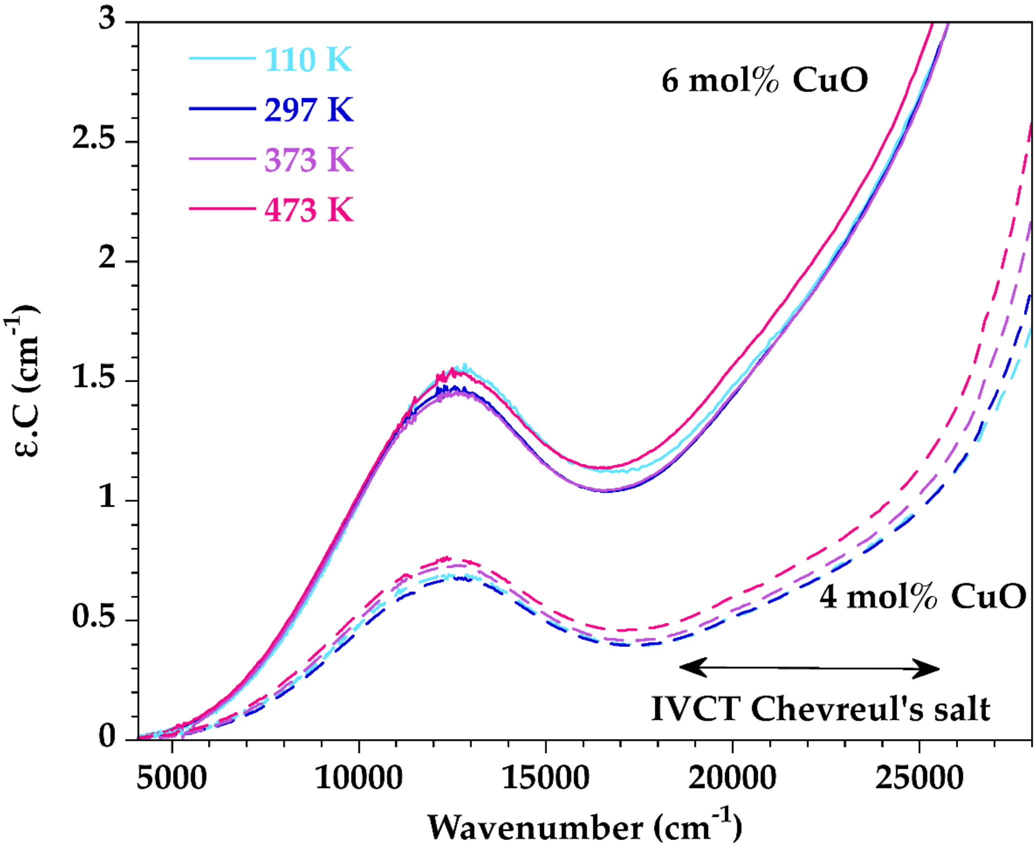

__Figure 12.__ Variation with temperature of the optical absorption spectra for SiAlCu$_x$ glasses with x = 4 and 6 mol% CuO. The horizontal arrow indicates the region in which IVCT is observed in Chevreul's salt [38], [39].

It is crucial to recognize that IVCT requires the close proximity of the involved ions, implying that the oxygen polyhedra surrounding them should preferentially share an edge or a face. An example of this is observed in Chevreul's salts, where there is an edge-sharing between the Cu^{2+} octahedron and the Cu^{+} tetrahedron [73]. In the context of copper ions in glasses, the local geometries of Cu^{2+} and Cu^{+} ions are discussed in §2.1. Cu^{2+} ions are surrounded by an elongated octahedron of oxygen atoms while Cu^{+} are suggested to have a linear twofold coordination, though distorted environments are also proposed. Therefore, if the presence of IVCT were to be confirmed, it would raise questions about the connectivity of oxygens surrounding the Cu^{2+}-Cu^{+} ion pair.

6. Discussion

The aim of this study is to understand the origin of the color variations in different types of glasses. Our observations allow us to identify various parameters that could affect coloration: the distortion of the Cu^{2+} site, the copper redox state, and the existence of Cu clustering.

6.1 Effects of Cu^{2+} site distortions

For all glazes, the Cu^{2+} absorption band was successfully fitted using three Gaussian functions, with intensities that roughly correspond to the expected electronic structure in an elongated octahedron (Figure S13). An adjustment with only two Gaussian functions was not satisfactory. The degrees of distortion (T) do not follow a specific trend (Table 5). There appears to be no clear correlation with changes in coloration. The measured T distortions are significant compared to those previously found in sodium-calcium silicates [32] or phosphate glasses [1], where they range between T = 0.69 and 0.78. Furthermore, there is a considerable variability in the characteristics of the Gaussian peaks calculated for EPT-27ter melted at 880 °C and 1250 °C, even though the glass composition is strictly identical, and the optical spectra overlap well in the region 5,000 17,500 cm^{-1}.

Based on the EPR spectra (Figure 7a), we postulated rhombic deformation, which is less symmetrical than axial elongation, for all glasses except BX9. With this hypothesis, we were able to calculate spectra that reasonably correspond to the experimental one. The EPR parameters (Table 6) calculated for BX9 and in *x* and *z* directions for other compositions are similar to those found in studies on Cu^{2+} sites in sodium silicates [5], [19], [74], which include $g_{\parallel}$ = 2.325 and $g_{\perp}$ = 2.06. Previous studies also observed spectra with a broad and intense band between 3,000 and 3,250 G [19], [63]. They noted its appearance when varying the total copper concentration in the glass. Sreekanth Chakradhar observes this band from 2.0 mol% CuO added to barium silicates [63], while Andronenko found it noticeable around 3 mol% CuO added to sodium silicates [19]. Both studies interpreted this band not as the effect of rhombic distortion but as the appearance of copper clusters. Andronenko modeled the EPR spectrum for 10 mol% copper by summing two contributions: (1) one corresponding to individual Cu^{2+} ions in axial symmetry, within an elongated octahedron, with $g_{\parallel}$ = 2.35, $g_{\perp}$ = 2.075, and (2) the other corresponding to copper clusters, with $g_{\parallel}$ = 2.35, $g_{\perp}$ = 2.15. This last value of $g_{\perp}$ is close to the g_y found by adjusting EPR spectra with rhombic symmetry. It is noteworthy that this broad band is only present in the glazes from Sevres containing more than 2 mol% CuO, i.e. all except BX9.

It is well recognized that the glass matrix can influence the position of the Cu^{2+} absorption band (see §2); however, its effect is unlikely to play a decisive role in the change from blue to green coloration. For instance, Bae and Weinberg did not observed a noticeable change in the peak position of the Cu^{2+} absorption band, even though the color changed under various melting and annealing conditions, which modified the copper redox state [1].

6.2 Copper redox state

The EPR quantification of the copper oxidation state in CCPNs and EPT-27ter shows variations that appear to correlate with color (Figure 7b). Specifically, at lower $\frac{[Cu^{2+}]}{[Cu_{tot}]}$ ratios, the UV band becomes more prominent relative to the Cu^{2+} band, resulting in a shift towards green hues. This UV band is primarily attributed to Cu^{+} absorption [7], indicating a relationship between color and the oxidation state of copper. Notably, redox analysis can account for the color variation between the EPT-27ter samples melted at 880 °C and 1250 °C. Despite having the same composition, the EPR redox ratio for EPT-27ter-1250°C is lower than that of EPT-27ter-880°C, which explains the shift of the UV edge towards lower energies and the resulting greener coloration.

BX9 distinguishes itself from other glazes in terms of the relationship between the UV optical absorption band and the proportion of Cu^+ it contains. Specifically, it is the composition for which the Cu^{2+} absorption band is the most shifted towards higher energies. Although the $\frac{[Cu^{2+}]}{[Cu_{tot}]}$ ratio is similar to those of CCPNs, BX9 appears turquoise instead of green. In optical spectroscopy, it is observed that its UV band becomes prominent only after 25,000 cm^{-1}, significantly differing from the CCPNs, where the UV band extend widely into the visible range. Hence, the Cu^+ concentration is not the sole factor to consider.

6.3 Importance of copper clustering on the glass coloration

In the optical absorption spectra (Figure 5 and Figure 8), the absorption near the UV region varies significantly with the composition of the glasses. For blue glasses (BX9 and EPT-27ter), the UV absorption band becomes prominent only after 25,000 cm^{-1}. In contrast, CCPN-16, CCPN-17 and $SiAlCu_x$ glasses containing copper proportions above ~2 mol% CuO exhibit a significant contribution between 18,000-27,000 cm^{-1}, thus shifting the minimum absorption towards lower energies. Rather than a change in the Cu^{2+} absorption band, this contribution in the violet-blue region appears to influence strongly the shape of the minimum absorption and its position.

This broad band position does not correspond to absorptions by Cu^+ which occurs at higher energy, and BX9, with its high Cu^+ content, does not exhibit this contribution. The shape of this broad band resembles that observed in obsidians between 14,000-22,000 cm^{-1} that has been assigned to Fe^{2+}-Fe^{3+} IVCT through optical absorption spectroscopy at low temperatures [44]. Such transitions are facilitated by the organization of iron into clusters, forming nanodomains resembling the crystallization of magnetite. Similarly, the broad contribution between 18,000-27,000 cm^{-1} could be attributed to the Cu^{2+}-Cu^+ IVCT, with an intensity proportional to the concentration of different pairs of valence ions that are in close proximity. This IVCT is important when the Cu^+ content and /or the total CuO content is high in CCPNS and $SiAlCu_x$ glasses. The occurrence of copper clusters is consistent with our EPR signals and previous studies [1], [43], confirming the impact of cation clustering of glass properties [75].

Glass composition appears to strongly influence the copper distribution and, consequently, the coloration. Glasses in SiAl-Cu_x series do not show a significant blue hue even at low copper content. The presence of Al_2O_3 (also in CCPNs) influences the redox state, favoring the reduced state, and could additionally impact the copper distribution, though a specific study is required to confirm this hypothesis. The BX9 sample appear atypical as its Cu^+ content is similar to CCPNs. This different behavior is likely related to the presence of boron in this compound as it has been shown that boron prevents cluster formation [67]. Although the EPT-27ter samples have a high CuO content, they do not exhibit a contribution attributable to IVCT. As EPT27-ter is a lead-bearing silicate glass, we could expect that lead could have an effect on the copper distribution, similar to boron. Notably, a similar color variation from blue to green is observed with increasing CuO content in lead and zinc-copper borate glasses [43].

7. Conclusions

The study focused on the blue and green colorations induced by copper in silicate glasses of various compositions. Optical absorption and EPR spectroscopies were used to gain insight into the phenomena influencing the perceived color based on the glass compositions and heat treatments. Optical absorption spectra analysis revealed that changes in color were primarily associated with variations in near-UV absorbance. Although there were small variations in the Cu^{2+} absorption band, they were considered insufficient to significantly impact the overall color. The color variations are correlated with the $\frac{[Cu^{2+}]}{[Cu_{tot}]}$ ratios determined by EPR. We consider that the minimum absorption in the visible spectrum, close to the UV, originated from electronic transitions involving Cu^+. However, discrepancies between the determination of Cu^{2+} and Cu^+ ions by EPR raised questions about the sole contribution of Cu^+ to the UV absorption front.

The EPR spectra for Cu^{2+} provide insight into the geometry of the site occupied by these ions. One of the spectra (BX9) suggests an axial geometry, corresponding to a tetragonally distorted octahedral site, as expected. The appearance of the other spectra, featuring a broad band in their central part, suggest two possible interpretations. Firstly, this appearance may be attributed to the rhombic deformation of the octahedron. Simulations of EPR spectra support this hypothesis, as simulations closely resembles the experimental spectra. However, the Cu^{2+} site described in the literature is still considered to be an octahedron with axial distortion. Secondly, the presence of copper clusters could have a similar effect on the spectrum. The correlation between the increase in copper concentration and the appearance of this broad band supports this hypothesis: in BX9, copper dilution prevents the formation of clusters; for CCPNs, which are more concentrated, the EPR band corresponding to clusters begins to appear; it becomes more obvious for the EPT-27ter, which contain even more copper.

Glasses with copper content above ~2 mol% CuO exhibit a broad absorption band between 18,000-27,000 cm^{-1}, giving a green hue. This band, attributed to Cu^{2+}-Cu^+ IVCT, is the primary reason for the change in coloration from blue to green in glasses. The presence of boron in BX9 prevents cluster formation, differentiating its behavior despite similar Cu^+ content to CCPNs. High CuO content in EPT-27ter does not exhibit IVCT, suggesting lead may influence copper distribution, warranting further study on lead glasses.

Data availability statement

Data of presented results can be provided upon request.

Underlying and related material

Supplementary materials are available at. https://doi.org/10.5281/zenodo.13165792.

Author contributions

Laurent Cormier: Conceptualization, Funding acquisition, Investigation, Methodology, Supervision, Writing – Original Draft. Cécile Noirot: Conceptualization, Formal Analysis, Investigation, Methodology, Writing – Original Draft.

Competing interests

The authors declare that they have no competing interests.

Acknowledgement

We are deeply indebted to Olivier Dargaud at the Cité de la Céramique - Sèvres for his invaluable discussions at the origin of this project and to Atika Chemmi, currently head of the Service of Applied Research of the Cité de la Céramique. The preliminary results were obtained during the M2 internship of Roland Mahayri, whose contributions are warmly acknowledged. Our gratitude extends to SOLEIL for provision of synchrotron radiation facilities and we would like to thank Nicolas Trcera for assistance in using beamline LUCIA (proposal 20201577) and Emiliano Fonda for assistance in using beamline SAMBA (proposal 20200932).

References

[1] B.-S. Bae and M. C. Weinberg, “Optical absorption of copper phosphate glasses in the visible spectrum,” Journal of Non-Crystalline Solids, vol. 168, pp. 223–231, 1994, doi: 10.1016/0022-3093(94)90333-6.

[2] S. Banerjee and A. Paul, "Chemical determination of copper, copper(I) and copper(II) in a borate glass,” Analytica Chimica Acta, vol. 68, pp. 226-230, 1974.

[3] G. Calas, N. Capobianco, and L. Galoisy, “Spectroscopic properties of alkali borate glasses containing Cu2+,” Journal of Non-Crystalline Solids, vol. 591, 121711, 2022, doi: 10.1016/j.jnoncrysol.2022.121711.

[4] G. Calas, L. Galoisy, and L. Cormier, “The color of glass,” in Encyclopedia of Glass Science, Technology, History, and Culture, 1st ed., P. Richet, R. Conradt, A. Takada, J. Dyon (Eds.), Wiley, 2021, ch. 6.2, pp. 677-691, doi: 10.1002/9781118801017.ch6.2.

[5] S. La Delfa, E. Ciliberto, and L. Pirri, “Behaviour of copper and lead as chromophore elements in sodium silicate glasses,” Journal of Cultural Heritage, vol. 9, e117–e122, 2008, doi: 10.1016/j.culher.2008.07.006.

[6] A. Silvestri, S. Tonietto, F. D’Acapito, and G. Molin, “The role of copper on colour of palaeo-Christian glass mosaic tesserae: An XAS study,” Journal of Cultural Heritage, vol. 13 , pp. 137–144, 2012, doi: 10.1016/j.culher.2011.08.002.

[7] T. Volotinen, “Mathematical description of absorbance spectra for Fe and Cu doped soda-lime-silica glasses,” PhD Thesis, University of Sheffield, 2007.

[8] G. Artioli, I. Angelini, and A. Polla, “Crystals and phase transitions in protohistoric glass materials,” Phase Transitions, vol. 81, pp. 233-252, 2008, doi: 10.1080/01411590701514409.

[9] G. Dardeniz, T. Yıldırım, C. Yıldırım, and E. Çiftçi, “Techniques of blue, green, and white faience bead production used at the early Bronze Age central Anatolian site of Resuloğlu (Turkey),” Archaeometry, vol. 63, pp. 327-342, 2021, doi: 10.1111/arcm.12606.

[10] A. S. Rodler, S. Klein, G. Artioli, and C. Brøns, “Probing the provenance of archaeological glaze colorants: Polychrome faunal reliefs of the Ishtar Gate and the Processional Way of Babylon: Probing the provenance of archaeological glaze colorants,” Archaeometry, vol. 61, pp. 837-855, 2019, doi: 10.1111/arcm.12455.

[11] I. C. Freestone, C. P. Stapleton, and V. Rigby, “The production of red glass and enamel in the Late Iron Age, Roman and Byzantine periods“, in Through a Glass Brightly. Studies in Byzantine and Medieval Art and Archaeology Presented to David Buckton, C. Entwistl (ed.), Oxbow Books, Oxford, pp. 142–154, 2003.

[12] C. Noirot, “Colorations rouge et orange de verres et glaçures sur céramique : étude du redox et de la cristallisation du cuivre,” PhD Thesis, Sorbonne University, 2022.

[13] C. Noirot, L. Cormier, N. Schibille, N. Menguy, N. Trcera, and E. Fonda, “Comparative investigation of red and orange Roman tesserae: Role of Cu and Pb in colour formation,” Heritage, vol. 5, pp. 2628-2645, 2022, doi: 10.3390/heritage5030137.

[14] N. Capobianco, “La couleur des vitraux au XIIIe siècle - Étude chimique et spectroscopique,” PhD Thesis, Sorbonne University, 2018.

[15] E. E. Khawaja, M. N. Khan, A. A. Kutub, and C. A. Hogarth, “Some electrical and optical properties of copper-sodium-phosphate glasses,” International Journal of Electronics, vol. 58, pp. 471-475, 1985, doi: 10.1080/00207218508939043.

[16] L. Verger, O. Dargaud, M. Chassé, N. Trcera, G. Rousse, and L. Cormier, “Synthesis, properties and uses of chromium-based pigments from the Manufacture de Sèvres,” Journal of Cultural Heritage, vol. 30, pp. 26-33, 2018, doi: 10.1016/j.culher.2017.09.012.

[17] L. Verger, O. Dargaud, N. Menguy, D. Troadec, and L. Cormier, “Interaction between Cr-bearing pigments and transparent glaze: A transmission electron microscopy study,” Journal of Non-Crystalline Solids, vol. 459, pp. 184-191, 2017, doi: 10.1016/j.jnoncrysol.2017.01.016.

[18] A. d’Albis, “Traité de la porcelaine de Sèvres,” Faton, Dijon, France, 2003.

[19] S. I. Andronenko, R. R. Andronenko, A. V. Vasil’ev, and O. A. Zagrebel’nyi, “Local symmetry of Cu2+ ions in sodium silicate glasses from data of EPR spectroscopy,” Glass

Physics and Chemistry, vol. 30, pp. 230-235, 2004, doi: 10.1023/B:GPAC.0000032224.23793.8c.

[20] A. Durán and J. M. Fernández Navarro, “The colouring of glass by Cu2+ ions,” Physics and Chemistry of Glasses, vol. 26, pp. 126-131, 1985.

[21] L. Grund Bäck, S. Ali, S. Karlsson, L. Wondraczek, and B. Jonson, “X-ray and UV-Vis-NIR absorption spectroscopy studies of the Cu(I) and Cu(II) coordination environments in mixed alkali-lime-silicate glasses,” Journal of Non-Crystalline Solids: X, vol. 3, pp. 100029, 2019, doi: 10.1016/j.nocx.2019.100029.

[22] K. Kamiya, K. Okasaka, M. Wada, H. Nasu, and T. Yoko, "Extended X-ray absorption fine structure (EXAFS) study on the local environment around copper in low thermal expansion copper aluminosilicate glasses,” Journal of the American Ceramic Society, vol. 75, pp. 477-478, 1992, doi: 10.1111/j.1151-2916.1992.tb08205.x.

[23] C. Maurizio, F. d’Acapito, M. Benfatto, S. Mobilio, E. Cattaruzza, and F. Gonella, "Local coordination geometry around Cu+ and Cu2+ ions in silicate glasses: an X-ray absorption near edge structure investigation,” The European Physical Journal B, vol. 14, pp. 211-216, 2000, doi: 10.1007/s100510050122.

[24] A. Santagostino Barbone, E. Gliozzo, F. D’Acapito, I. Memmi Turbanti, M. Turchiano, and G. Volpe, "The sectilia panels of Faragola (Ascoli-Satriano, soutern Italy): a multi-analytical study of the red, orange and yellow glass slabs,” Archaeometry, vol. 50, pp. 451-473, 2008, doi: 10.1111/j.1475-4754.2007.00341.x.

[25] R. Debnath and S. K. Das, “Site-dependent luminescence of Cu+ ions in silica glass,” Chemical Physics Letters, vol. 155, pp. 52-58, 1989, doi: 10.1016/S0009-2614(89)87359-2.

[26] J. Lee, T. Yano, S. Shibata, A. Nukui, and M. Yamane, "EXAFS study on the local environment of Cu+ ions in glasses of the Cu2O-Na2O-Al2O3-SiO2 system prepared by Cu+/Na+ ion exchange,” Journal of Non-Crystalline Solids, vol. 277, pp. 155-161, 2000, doi: 10.1016/S0022-3093(00)00330-6.

[27] J. Kaufmann and C. Rüssel, "Diffusion of copper in soda-silicate and soda-lime-silicate melts,” Journal of Non-Crystalline Solids, vol. 356, pp. 1158-1162, 2010, doi: 10.1016/j.jnoncrysol.2010.03.015.

[28] R. G. Burns, "Mineralogical applications of crystal field theory,” 2nd ed., Cambridge University Press, 1993, doi: 10.1017/CBO9780511524899.

[29] M. Cable and Z. D. Xiang, "The optical spectra of copper ions in alkali-lime-silica glasses,” Physics and Chemistry of Glasses, vol. 33, pp. 154-160, 1992.

[30] M. O. J. Y. Hunault and C. Loisel, "Looking through model medieval green glasses: From color to recipe,” Int. J. Appl. Glass Sci., vol. 11, pp. 463-470, 2020, doi: 10.1111/ijag.15134.

[31] Z. Zhou, A. Navrotsky, and D. S. McClure, "Oxidation states of copper in lead borate glass,” Physics and Chemistry of Glasses, vol. 34, pp. 251-254, 1993.

[32] L. Grund Bäck, "Redox reactions and structure - properties relations in mixed alkali/alkaline earth silicate glasses - The role of antimony oxides during the fining process - A structural study of copper(I) and copper(II),” PhD Thesis, Linnaeus University, 2015.

[33] Y. Fujimoto and M. Nakatsuka, "Spectroscopic properties and quantum yield of Cu-doped SiO2 glass,” Journal of Luminescence, vol. 75, pp. 213-219, 1997, doi: 10.1016/S0022-2313(97)00121-X.

[34] S. Gómez, I. Urra, R. Valiente, and F. Rodríguez, "Spectroscopic study of Cu2+/Cu+ doubly doped and highly transmitting glasses for solar spectral transformation,” Solar Energy Materials and Solar Cells, vol. 95, pp. 2018-2022, 2011, doi: 10.1016/j.solmat.2010.07.022.

[35] K. Tanaka, T. Yano, S. Shibata, M. Yamane, and S. Inoue, "Cu+-doped CaO-P2O5 glasses for lasers,” Journal of Non-Crystalline Solids, vol. 178, pp. 9-14, 1994, doi: 10.1016/0022-3093(94)90258-5.

[36] J. C. Zhang, B. Moine, C. Pedrini, C. Parent, and G. Flem, "Optical spectroscopy of monovalent copper-doped borate glasses,” Journal of Physics and Chemistry of Solids, vol. 51, pp. 933-939, 1990, doi: 10.1016/0022-3697(90)90035-E.

[37] A. N. Pestryakov, V. P. Petranovskii, A. Kryazhov, O. Ozhereliev, N. Pfänder, and A. Knop-Gericke, "Study of copper nanoparticles formation on supports of different nature by UV–Vis diffuse reflectance spectroscopy," Chemical Physics Letters, vol. 385, pp. 173-176, 2004, doi: 10.1016/j.cplett.2003.12.077.

[38] M. Inoue, H. Grijalva, M. B. Inoue, and Q. Fernando, "Spectroscopic and magnetic properties of Chevreul's salt, a mixed valence copper sulfite Cu3(SO3)2·2H2O," Inorganica Chimica Acta, vol. 295, pp. 125-127, 1999, doi: 10.1016/S0020-1693(99)00333-3.

[39] L. A. da Silva, J. B. de Andrade, and H. E. Toma, "Electronic spectra of Chevreul's salts," J. Braz. Chem. Soc., vol. 13, pp. 624-628, 2002, doi: 10.1590/S0103-50532002000500013.

[40] B. Bae and M. C. Weinberg, "Ultraviolet optical absorptions of semiconducting copper phosphate glasses," Journal of Applied Physics, vol. 73, pp. 7760-7766, 1993, doi: 10.1063/1.353975.

[41] J. Simonetti and D. S. McClure, "The 3 d → 4 p transitions of Cu+ in LiCl and of transition-metal ions in crystals," Phys. Rev. B, vol. 16, pp. 3887-3892, 1977, doi: 10.1103/PhysRevB.16.3887.

[42] P. Boutinaud, C. Parent, G.L. Flem, C. Pedrini, and B. Moine, "Spectroscopic investigation of the copper (I)-rich phosphate CuZr2(PO4)3," J. Phys.: Condens. Matter, vol. 4, pp. 3031-3042, 1992, doi: 10.1088/0953-8984/4/11/026.

[43] Z. Y. Yao, D. Möncke, E. I. Kamitsos, P. Houizot, F. Célarié, T. Rouxel, and L. Wondraczek, "Structure and mechanical properties of copper–lead and copper–zinc borate glasses," Journal of Non-Crystalline Solids, vol. 435, pp. 55-68, 2016, doi: 10.1016/j.jnoncrysol.2015.12.005.

[44] L. Galoisy and G. Calas, "The unique speciation of iron in calc-alkaline obsidians," Chemical Geology, vol. 559, pp. 119925, 2021, doi: 10.1016/j.chemgeo.2020.119925.

[45] S. M. Mattson and G. R. Rossman, "Identifying characteristics of charge transfer transitions in minerals," Phys. Chem. Minerals, vol. 14, pp. 94-99, 1987, doi: 10.1007/BF00311152.

[46] M. Cable and Z. D. Xiang, "Cuprous-cupric equilibrium in soda-lime-silica glasses melted in air," Physics and Chemistry of Glasses, vol. 30, pp. 237-242, 1989.

[47] A. Durán and F.J. Valle, "Analysis of the different states of oxidation of copper in glasses: redox equilibrium," Glass Technol., vol. 26, pp. 179-185, 1985.

[48] J. A. Jiménez, "Absorption spectroscopy analysis of calcium-phosphate glasses highly doped with monovalent copper," ChemPhysChem, vol. 17, pp. 1642-1649, 2016, doi: 10.1002/cphc.201600026.

[49] J. Kaufmann and C. Rüssel, "Redox behavior and diffusion of copper in soda-lime-silica melts," Journal of Non-Crystalline Solids, vol. 354, pp. 4614-4619, 2008, doi: 10.1016/j.jnoncrysol.2008.05.046.

[50] H. D. Schreiber, B. K. Kochanowski, C. W. Schreiber, A. B. Morgan, M. T. Coolbaugh, and T. G. Dunlap, "Compositional dependence of redox equilibria in sodium silicate glasses," Journal of Non-Crystalline Solids, vol. 177, pp. 340-346, 1994, doi: 10.1016/0022-3093(94)90548-7.

[51] F. G. K. Baucke and J. A. Duffy, "The effect of basicity on redox equilibria in molten glasses," Physics and Chemistry of Glasses, vol. 32, pp. 211-218, 1991.

[52] S. P. Singh, G. Prasad, and P. Nath, "Kinetic study of Cu+-Cu2+ equilibrium in sodium Na2O-Al2O3-B2O3 glass," Journal of the American Ceramic Society, vol. 61, pp. 377-379, 1978, doi: 10.1111/j.1151-2916.1978.tb09340.x.

[53] S. P. Singh and A. Kumar, "Molar extinction coefficients of the cupric ion in silicate glasses," Journal of Materials Science, vol. 30, pp. 2999-3004, 1995, doi: 10.1007/BF00349674.

[54] M. Maggetti and A. D'Albis, "Phase and compositional analysis of a Sèvres soft paste porcelain plate from 1781, with a review of early porcelain techniques," European Journal of Mineralogy, vol. 29, pp. 347-367, 2017, doi: 10.1127/ejm/2017/0029-2627.

[55] P. Kubelka and F. Munk, "Ein Beitrag zur Optik der Farbanstriche," Z. Techn. Phys., vol. 12, pp. 593-601, 1931.

[56] G. R. Eaton, S. S. Eaton, D. P. Barr, and R. T. Weber, "Quantitative EPR“, Springer Vienna, Vienna, 2010, doi: 10.1007/978-3-211-92948-3.

[57] E. Fonda, A. Rochet, M. Ribbens, L. Barthe, S. Belin, and V. Briois, "The SAMBA quick-EXAFS monochromator: XAS with edge jumping,” Journal of Synchrotron Radiation, vol. 19, pp. 417-424, 2012, doi: 10.1107/S0909049512009703.

[58] J. A. Bearden and A. F. Burr, "Reevaluation of X-Ray atomic energy levels,” Rev. Mod. Phys., vol. 39, pp. 125-142, 1967, doi: 10.1103/RevModPhys.39.125.

[59] B. Ravel and M. Newville, "ATHENA, ARTEMIS, HEPHAESTUS: data analysis for X-ray absorption spectroscopy using IFEFFIT,” Journal of Synchrotron Radiation, vol. 12, pp. 537-541, 2004, doi: 10.1107/S0909049505012719.

[60] D. Vantelon, N. Trcera, D. Roy, T. Moreno, D. Mailly, S. Guilet, E. Metchalkov, F. Delmotte, B. Lassalle, P. Lagarde, and A.-M. Flank, "The LUCIA beamline at SOLEIL,” Journal of Synchrotron Radiation, vol. 23, pp. 635-640, 2016, doi: 10.1107/S1600577516000746.

[61] P. Thakur, V. Bisogni, J.C. Cezar, N. B. Brookes, G. Ghiringhelli, S. Gautam, K. H. Chae, M. Subramanian, R. Jayavel, and K. Asokan, "Electronic structure of Cu-doped ZnO thin films by x-ray absorption, magnetic circular dichroism, and resonant inelastic x-ray scattering,” Journal of Applied Physics, vol. 107, pp. 103915, 2010, doi: 10.1063/1.3372758.

[62] S. Stoll and A. Schweiger, "EasySpin, a comprehensive software package for spectral simulation and analysis in EPR,” Journal of Magnetic Resonance, vol. 178, pp. 42-55, 2006, doi: 10.1016/j.jmr.2005.08.013.

[63] R. P. Sreekanth Chakradhar, A. Murali, and J. L. Rao, “Electron paramagnetic resonance and optical absorption studies of Cu2+ ions in alkali barium borate glasses,” Journal of Alloys and Compounds, vol. 265, pp. 29-37, 1998, doi: 10.1016/S0925-8388(97)00437-4.

[64] T. H. Noh and E. Le Shim, "Study of CuO content on physical and structural properties of Li2O-B2O3-CuO glasses using electron paramagnetic resonance,” Journal of Non-Crystalline Solids, vol. 474, pp. 37-42, 2017, doi: 10.1016/j.jnoncrysol.2017.08.021.

[65] I. Ardelean, S. Cora, and D. Rusu, "EPR and FT-IR spectroscopic studies of Bi2O3-B2O3-CuO glasses,” Physica B: Condensed Matter, vol. 403, pp. 3682-3685, 2008, doi: 10.1016/j.physb.2008.06.016.

[66] I. Ardelean, O. Cozar, S. Filip, V. Pop, and I. Cenan, "EPR and magnetic susceptibility studies of Cu2+ ions in Bi2O3·GeO2 glasses,” Solid State Communications, vol. 100, pp. 609-613, 1996, doi: 10.1016/0038-1098(96)00472-3.

[67] F. Ciorcas, S. K. Mendiratta, I. Ardelean, and M. A. Valente, "Structural and magnetic studies of CuO-TeO2 and CuO-TeO2-B2O3 glasses,” Eur. Phys. J. B, vol. 20, pp. 235-240, 2001, doi: 10.1007/PL00022985.

[68] O. Cozar and I. Ardelean, "The local symmetry of Cu2+ ions in phosphate glasses,” Journal of Non-Crystalline Solids, vol. 92, pp. 278-281, 1987, doi: 10.1016/S0022-3093(87)80045-5.

[69] A. Dehelean, A. Popa, S. Rada, and E. Culea, "EPR and magnetic characterization of Fe2O3-TeO2 and CuO-TeO2 glasses obtained by melt quenching and sol–gel processes,” Journal of Magnetism and Magnetic Materials, vol. 381, pp. 131-137, 2015, doi: 10.1016/j.jmmm.2014.12.074.

[70] P. Bertrand, "La spectroscopie de résonance paramagnétique électronique: applications,” EDP sciences, Les Ulis, 2014.

[71] R. G. Burns, "Intervalence transitions in mixed valence minerals of iron and titanium,” Annu. Rev. Earth Planet. Sci., vol. 9, pp. 345-383, 1981, doi: 10.1146/annurev.ea.09.050181.002021.

[72] B. Scott and R. Willett, "Crystal structure and electronic spectroscopy of bis(hydrazinium) hexachlorotricuprate(2I,II): a copper(I)-copper(II) mixed-valence system exhibiting intervalence charge transfer,” Inorg. Chem., vol. 30, pp. 110-113, 1991, doi: 10.1021/ic00001a020.

[73] P. Kierkegaard, B. Nyberg, "The crystal structure of Cu2SO3.CuSO3.2H2O,” Acta Chem. Scand., vol. 19, pp. 2189-2199, 1965, doi: 10.3891/acta.chem.scand.19-2189.

[74] H. Hosono, H. Kawazoe, and T. Kanazawa, "ESR and optical absorption of cupric ion in borate glasses," Journal of Non-Crystalline Solids, vol. 34, pp. 339-356, 1979, doi; 10.1016/0022-3093(79)90021-8.

[75] L. Cormier, L. Galoisy, G. Lelong, and G. Calas, "From nanoscale heterogeneities to nanolites: cation clustering in glasses," Comptes Rendus. Physique, vol. 24, pp. 199-214, 2023, doi: 10.5802/crphys.150.

SUPPLEMENTARY DATA

Glass Europe Vol. 2 (2024) 55-81

https://doi.org/10.52825/glass-europe.v2i.1274

Understanding the influence of copper on the color of glasses and glazes: copper environment and redox

Laurent Cormier[1], Cécile Noirot[1]

[1] Sorbonne Université, Muséum National d'Histoire Naturelle, UMR CNRS 7590, IRD, Institut de Minéralogie, de Physique des Matériaux et de Cosmochimie, IMPMC, 75005 Paris, France

Copper-based pigments used at the Manufacture of Sèvres

Table S1. Copper-based pigments used at the Manufacture of Sèvres and referenced in d'Albis's book (d'Albis, 2003). The color corresponds to the description used at Sèvres.

	Color	Description	Number1	Number2	Page
Copper based pigment	Grey	$CuO + Fe_2O_3$, Mn_3O_4,Co_3O_4, NiO	10.132	1.298.61	211
Colored gold	red	CuO + Au (powder) the flux is bismuth sub-nitrate, $BiONO_3H_2O$			265
Colored underglaze for hard paste (CCPN = couverte colorée de pâte nouvelle)	**Dark green**	See below Table S2	**16**	**1.46.99**	300
	Green water	See below Table S2	**17**	**1.81.89**	300
	Dark green	Based on CCPN-16	25	1.200.90	300
	Turquoise celadon	CuO + uncolored underglaze + colored underglaze with Cr_2O_3	29	1.181.90	301
	Azur blue	CuO + uncolored underglaze + fritt with CoO	45	2.123.57	302
	Azur blue	Pigment 10.132 + uncolored underglaze + fritt with CoO	45 PC	1.11.77	302
	Blackish grey	CCPN-16 + pigments based on Fe and Mn	66	1.211.85	304
Glyceric colours	Fresh green	copper nitrate + glycerine	5	1.48.80	305
New paste enamels (émaux de pâte nouvelle)	Green enamel	CuO + hard paste underglaze + $Pb_3O_4 + SiO_2 + H_3BO_3$	19	1.17.55	308
	Green enamel	$CuO + SiO_2 + Pb_3O_4$	20 N	1.96.25	308
	Turquoise enamel	$CuO + SiO_2 + Pb_3O_4 + Na_2CO_3$	39 N	1.36.55	309
	Green celadon enamel	Pigment 20 N + pigment based on Fe	37 N		309
Background colors for soft paste	Yellow green	Copper chromate $CrCuO_4 + SiO_2 + Pb_3O_4$	9	1.329.26	315
	Olive green	$CuO + Fe_2O_3 + MnO$ + flux based on $SiO_2 + Pb_3O_4$	11	2.341.26	315
	Turquoise	CuO + flux based on $SiO_2 + Pb_3O_4$	12	2.301.46	315
	Light blue	CuO + CoO + flux based on $SiO_2 + Pb_3O_4$	13	1.155.92	315
	Blue 'lapis'	$CuO + CoO + SiO_2 + Pb_3O_4 + Na_2CO_3$	21	1.147.27	316
	Jade	$CuO + Fe_2O_3 + NiO$ + flux based on $SiO_2 + Pb_3O_4$	24	1.142.48	316

	Turquoise	See below Table S2	**27 Ter**	**1.313.88**	**316**
	Camellia green	CuO + Fe_2O_3 + flux based on SiO_2 + Pb_3O_4	29	1.330.26	316
	Emerald green	CuO + Fe_2O_3 + flux based on SiO_2 + Pb_3O_4	30	1.190.85	316
	Leek green	CuO + $PbCrO_4$ + flux based on SiO_2 + Pb_3O_4	31	1.109.45	316
	Theodore Deck Green	Pigment 30 + Pigment 27ter		1.69.85	317
	Vincennes green	Pigment 38 + Naples Yellow (lead antimonate)	38	2.33.89	317
	Turquoise for 38	CuO + H_3BO_3 + SiO_2 + Pb_3O_4 + Na_2CO_3			317
	Egyptian blue	CuO + pigment 13 + H_3BO_3 + SiO_2 + Pb_3O_4 + Na_2CO_3 + Li_2CO_3	39	1.351.85	317
Stoneware colors	Yellow Brown-Greenish Streaks	CuO + Fe_2O_3 + TiO_2 + flux	20 G	1.165.24	322
	Black brown	CuO + Fe_2O_3 + uncolored underglaze + flux	21 G	1.77.69	322
	Greenish blue	CuO + CoO + Fe_2O_3 + TiO_2 + flux	24 G	1.248.00	322

CCPN: The mixture consists of a colorless matrix and CuO as pigment (d'Albis, 2003).

Glyceric colors: color, developed in 1939, which consists of the solution in glycerin of soluble metal salts

Hard paste enamels: it is a color applied in thickness and fired at 950°C (petit feu) on hard porcelain baked with its underglaze

Stoneware colors: these colors are still in used for hard paste porcelains.

Table S2. Composition of the three glazes investigated, as described in d'Albis's book (d'Albis, 2003).

	CCPN-16 - 1.46.99	CCPN-17 - 1.81.89	EPT-27ter - 1.313.88
Copper oxide	401	201	53
Chalk	1273	1528	
Finland feldspar	4221	4231	
Quartz BS 15	2645	2733	458
Kaolin BIP	1460	1307	
Sodium carbonate83%			201
Minium			288
	10000	10000	1000

❖ Jahn Teller deformation

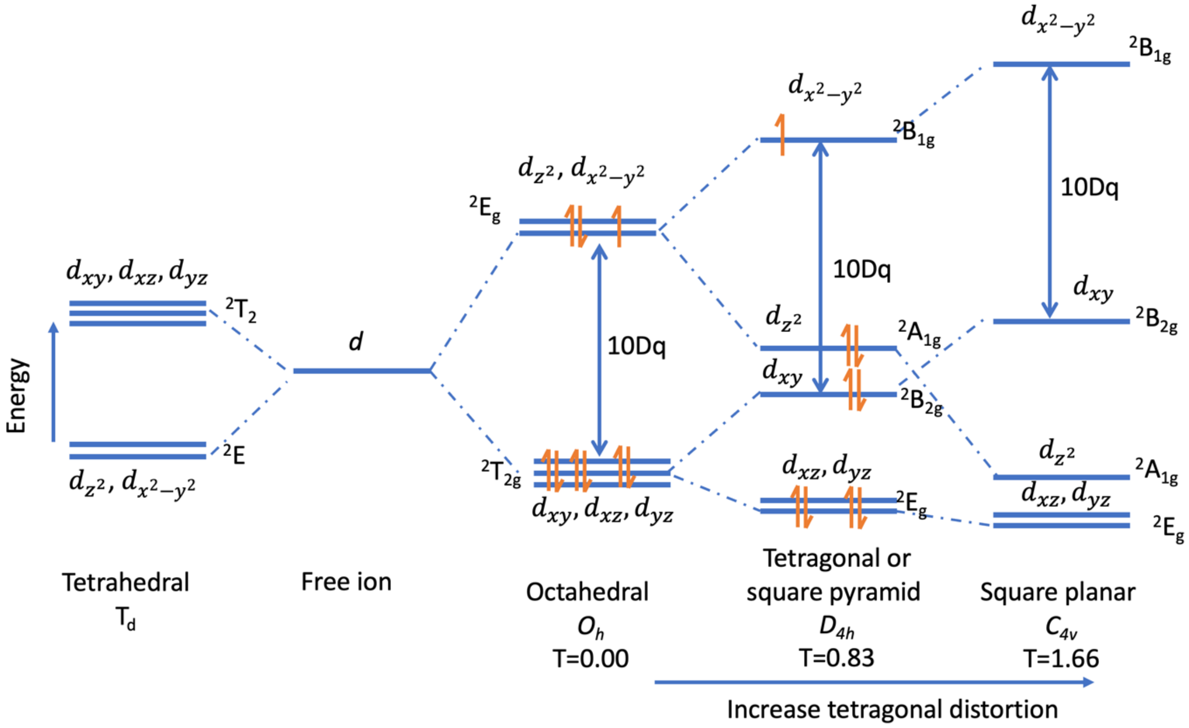

Figure S1. Energy level diagram of the Cu^{2+} ion in ligand fields with different symmetries.

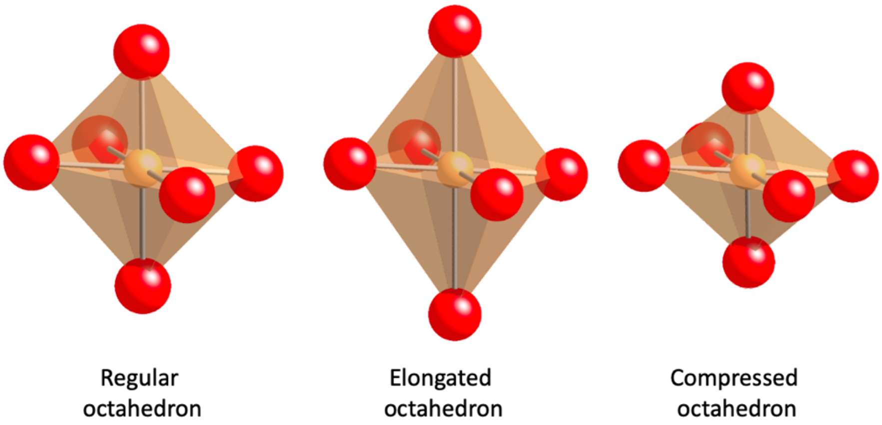

Figure S2. Representation of a perfect tetrahedron and Jahn-Teller distorted octahedra.

Characterization of CCPN pigments and glazes

Before applying the glaze to the degourdi porcelain (Figure S3a), it is essential to conduct an initial firing of the porcelain at 850 °C, with a gradual temperature increase of ~100 °C per hour. This step ensures that porcelain paste gains solidity while preserving the necessary porosity for the subsequent glaze application. The water content within the raw porcelain, including that inherent in the kaolin sheets, is eliminated during this stage, leading to porcelain shrinkage due to water loss. In Figure S3b, the glaze has been applied and is now ready for the firing process. The grayish hue results from the black copper oxide present in the decorative mixture. After the firing process (Figure S3c), the color becomes permanently fixed onto the porcelain.

New hard paste colored covers (CCPN, derived from the French term '*Couverte Colorée de Pâte Nouvelle*') are prepared by grinding a colorless component with a specific chemical composition for new hard paste, along one or more pigments (refer to Tables S1 and S2). The grinding duration is tailored to the desired decoration and has been optimized by the chemists at the Manufacture of Sèvres. The colorless component, a vitrified coating named CI (derived from the French term '*Composant Incolore*'), is obtained from a mixture of feldspar, quartz, chalk and kaolin. The chemical composition of CI for the pigments relevant to the current study is provided in Table S2, as compiled by d'Albis (d'Albis, 2003). The CI and pigment(s) mixture is ground for 10 minutes at 300 rpm. Subsequently, the water is evaporated in an oven at 70 °C, resulting in a powder. The CCPN powders are then ready for immediate use or can be stored for future applications at the Manufacture.

Figure S3. (a) Example of colored coating deposition. (b) pre-fired condition. (c) Glaze after firing.

The firing procedure to achieve the glaze involves several stages: an initial temperature increase up to 300 °C within 3 hours, followed by a second rise up to 850 °C in 5 hours, and a final increase to 1280 °C over 4.5 hours with a 15-minute plateau. The gradual temperature rise ensures even distribution of temperature, a crucial factor, especially in the case of large furnaces. Following this firing process, the furnace is turned off, allowing for a natural cooling process. This gradual cooling is essential to prevent stress on both the porcelain and its glaze. The kiln atmosphere is not controlled during the firing of CCPN; instead, it relies on the ambient, oxidizing air. This approach maintains an oxidizing atmosphere throughout the firing process.

X-ray diffraction (XRD) diagrams obtained on initial powders indicate that the mixture is predominantly amorphous. Identification of copper compounds is challenging, given the small amounts of CuO present, and only a weak Bragg peak attributed to unfused quartz is observed (Figure S4a). Following the firing process (Figure S4b), distinct Bragg peaks become visible. Given the highly fusible nature of the colorless glaze mixture, it is improbable that these peaks originate from the glaze itself, rather, they unquestionably result from the porcelain beneath the glaze. Similar to the starting mixture, no copper-related phases were detected.

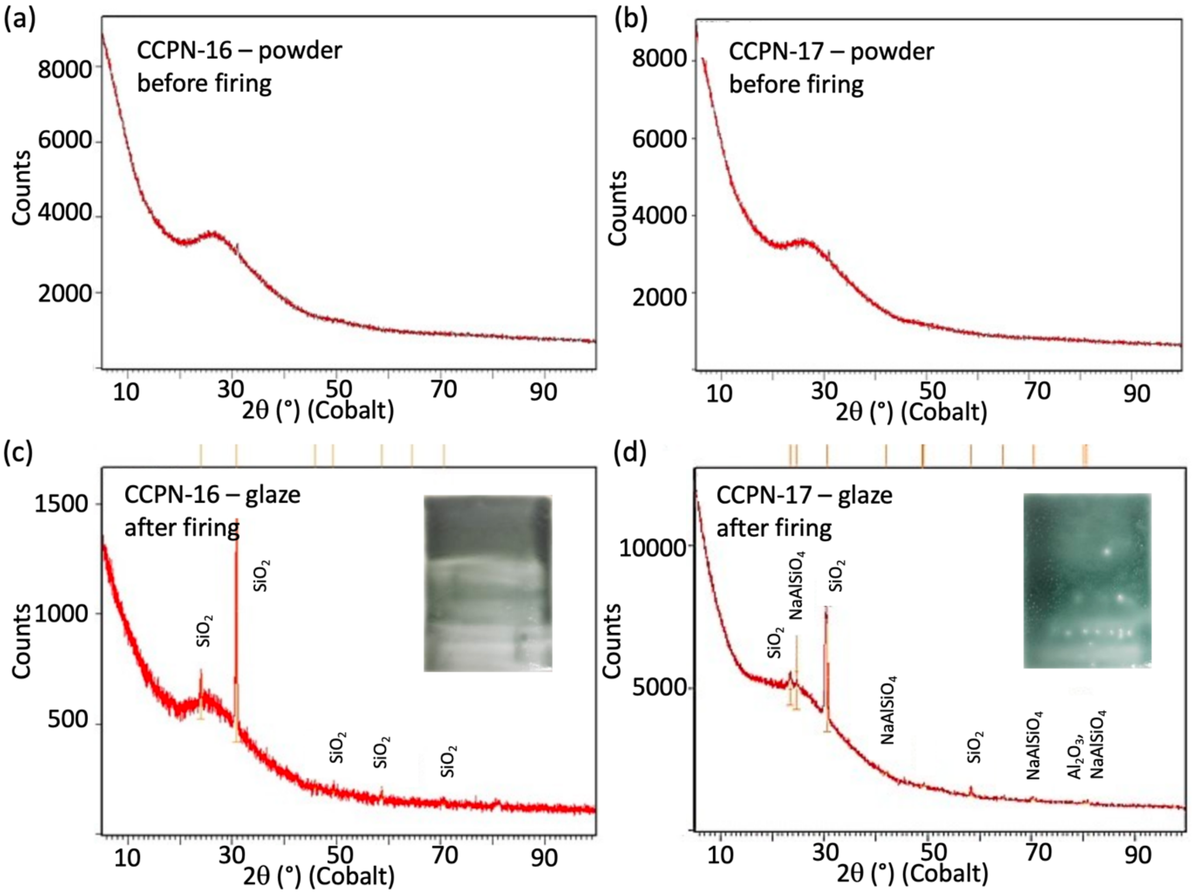

Figure S4. X-ray diffractograms of the initial powders of (a) CCPN-16 and (b) CCPN-17, prepared at the Manufacture of Sèvres. X-ray diffractograms of (c) the CCPN16 and (d) CCPN-17 glazes appplied on ceramic shards.

The glaze decorations were characterized using UV-visible spectroscopy. The diffuse reflectance spectra obtained were transformed into a remission function, F(r), through the application of the Kubelka-Munk formula (Kubelka and Munk, 1931).

Glaze decorations were applied in three different thicknesses to investigate the flaking limit of the enamel, while also exploring color hue variation with varying thickness. The optical absorption spectra corresponding to different thicknesses were normalized to the Cu^{2+} absorption peak near 12,600 cm^{-1} for comparative analysis. In the diffuse reflectance mode, absorption intensity varies with grain size and our focus is on relative intensities. Unless specified otherwise, optical absorption spectroscopy will always be performed on the thickest part of the enamel.

The spectrum of the initial pigment CCPN-16 (Figure S5a, green curve) reveals the presence of an absorption edge near 14,500 cm^{-1}. This edge corresponds to the absorption by copper oxide mixed with the colorless component CI. The spectrum for CCPN-16 glaze shows the emergence of a band in the visible range around 12,600 cm^{-1} (Figure S5a, red curve), explaining the green color and corresponding to Cu^{2+} ions occupying tetragonally distorted octahedral sites (refer to the main text). Absorption is lower for the region between 15,000 and 20,000 cm^{-1}. A second band appears in the near UV region around 27,000 cm^{-1} and extends towards the visible. Iron, present as an impurity in quartz, is the most likely candidate to explain the appearance of the UV band. At these energies, there are three absorption bands located near 22,800, 24,000 and 26,400 cm^{-1}, that are attributed to Fe^{3+} ions, and an intense oxygen-iron charge transfer band (Vercamer, 2016). This UV band also contains various contributions due to Cu^{+} and charge transfers (see main text). The glaze exhibits a green tint after firing above 1,100°C on the ceramic shard Figure S5b.

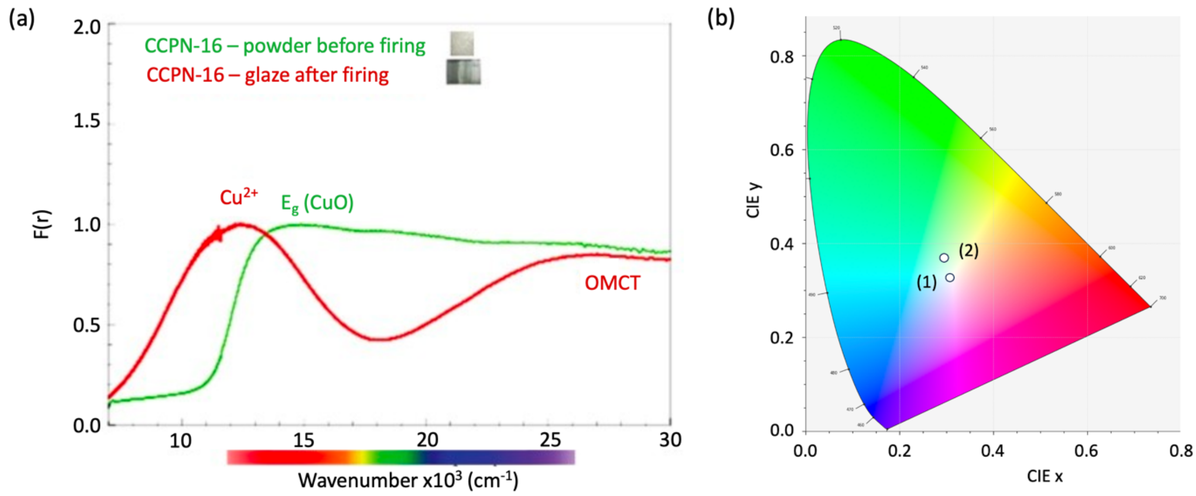

Figure S5. Optical spectroscopic results for CCPN-16. (a) Optical absorption spectra for the initial powder (green) and the glaze applied on the ceramic (red). (b) Chromaticity diagram, where pigment color coordinates are calculated from their diffuse reflectance spectra. Points 1 and 2 correspond to the initial powder and the glaze applied on the ceramic, respectively.

Figure S6 presents optical absorption spectra measured in three different regions corresponding to varying glaze thicknesses for CCPN-16. The Cu^{2+} band widens with increasing thickness and, consequently, with the intensity of the color (A > B > C).

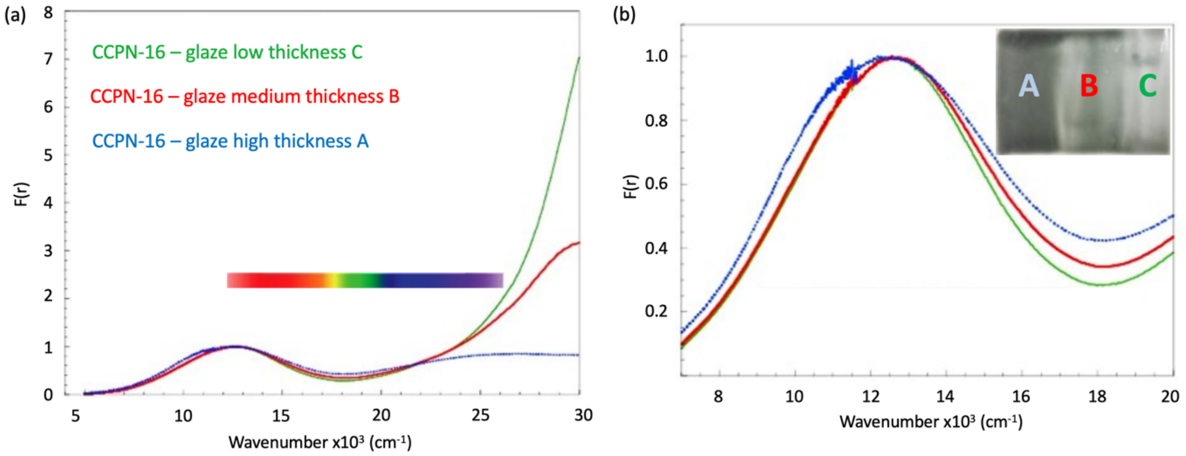

Figure S6. (a) Optical absorption spectra obtained on the three regions of the ceramic shard corresponding to varying thicknesses of the glaze. (b) Zoom on the Cu^{2+} absorption band.

CCPN-17 exhibits nearly identical characteristics to CCPN-16. Figure S7 shows the CuO absorption edge for the initial powder before firing and the two bands absorption bands in the glaze, primarily due to Cu^{2+} and charge transfer bands associated with Fe^{3+} and Cu^{+}. The thickness effect remains consistent with CCPN-16 in the broadening of the Cu^{2+} band, and it is not represented as it does not provide new information.

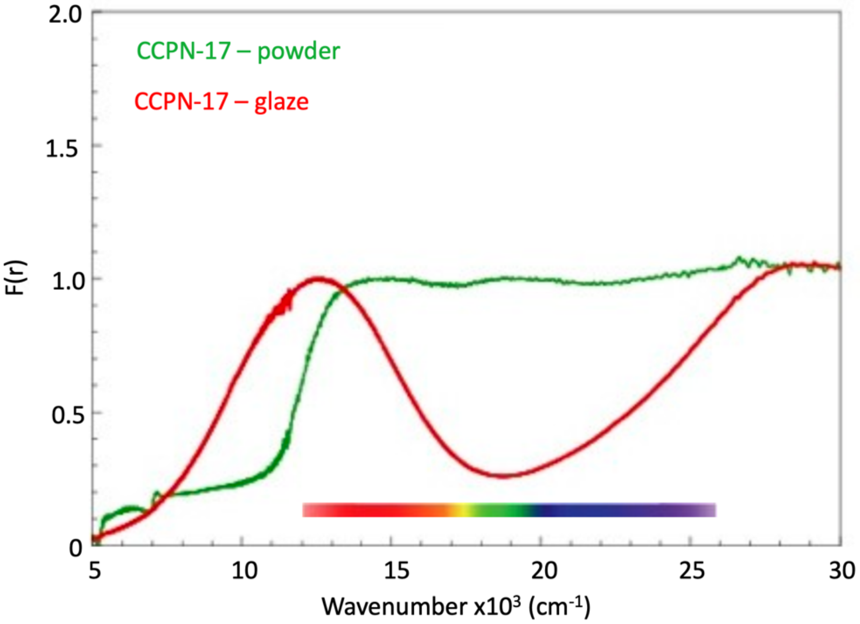

Figure S7. Optical absorption spectra for CCPN-17: initial powder (green) and the glaze applied on the ceramic (red).

❖ Characterization of EPT pigments and glazes

The glaze for the soft porcelain is predominantly composed of a lead silicate. To achieve aesthetic results after firing, it must be applied with a specific thickness. Given its tendency to flow on vertical surfaces, it is essential to include a refining stage at the end of the firing process. This additional step allows the glaze, especially in areas where it has accumulated, sufficient time to refine, facilitating the escape of air or gas bubbles. The glaze is fired at 880 °C, with a two-hour refining stage observed at the end of the firing process.

The third pigment mixture considered in the current study is the EPT-27ter, a lead silicate glass. Lead serves as a flux, aiding in the homogenization and diffusion of elements during the firing process. Table S2 provides the composition of the EPT-27ter.

The XRD diagram in Figure S8a shows that EPT-27ter has a completely amorphous structure as expected due to high fusibility of the lead silicate. In the optical spectrum of EPT-27ter (Figure S8b), two absorption bands are present, one centered at 12,700 cm^{-1} and another one at 28,600 cm^{-1}. The minimum absorption is distinctly localized in the blue region, differing from the CCPN glaze where the minimum was red-shifted, resulting in a greenish coloration.

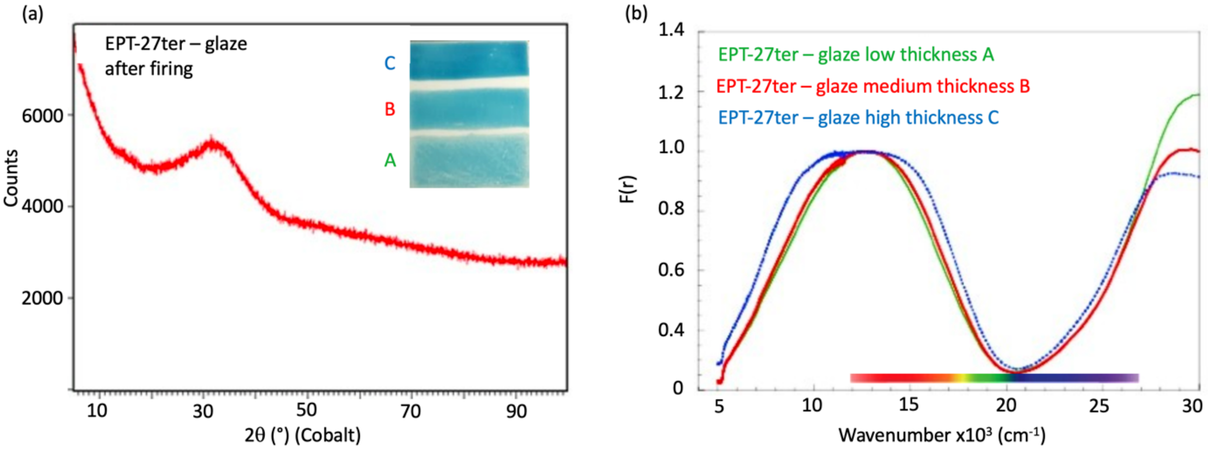

Figure S8. (a) X-ray diffractogram of the EPT-27ter glaze appplied on a ceramic shard. (b) Optical absorption spectra obtained on the three regions of the ceramic shard corresponding to varying thicknesses of the glaze.

To investigate the impact of melting temperature on the coloration of EPT-27ter, normally fired at 880 °C at Sèvres, the EPT-27ter mixture was remelted at 1250 °C in a platinum crucible for one hour. Following this heat treatment, the bottom of the crucible was immersed in water to quench the glass. Pieces of glass were then polished with parallel faces to avoid any background absorption. The optical absorption spectra in Figure S9a were obtained in transmission mode. It is observed that there is a sharp reduction in intensity when the firing temperature increase. The two bands are centered around 1200 cm^{-1}. On the chromaticity diagram it is noticeable that for melting at 1250 °C, there is a shift towards the green region, which is visually confirmed in the sample photos. The color variation in these two samples seems to result from both the variation in the Cu^{2+} absorption band and the UV band, indicating a different copper redox state. Lead-based glass exhibits a clearly distinct behavior from the CCPN samples.

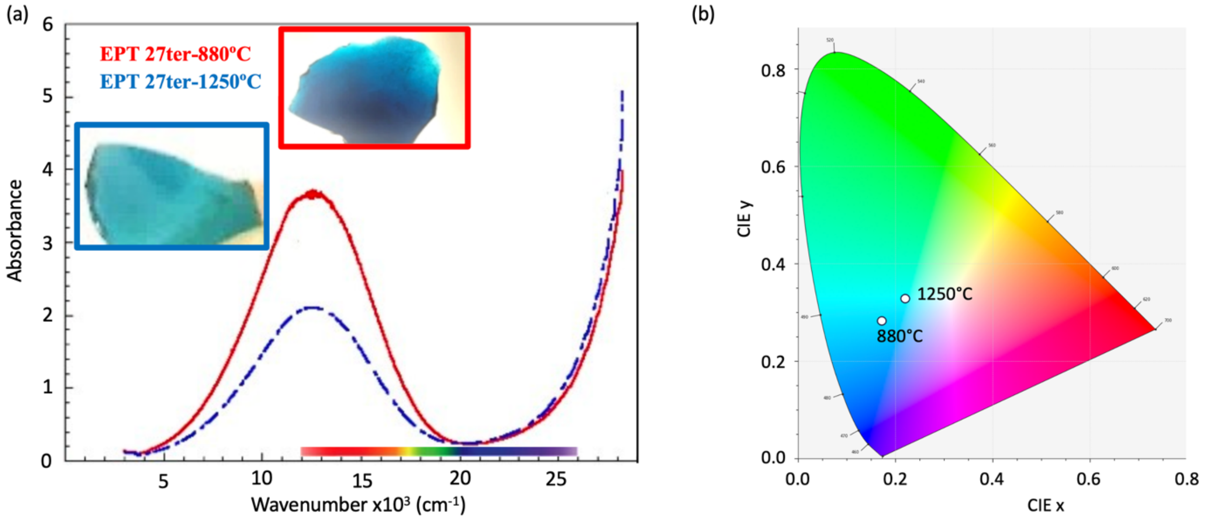

Figure S9. Effect of the melting temperature on (a) the optical absorption spectra and (b) the corresponding points in the chromaticity diagram.

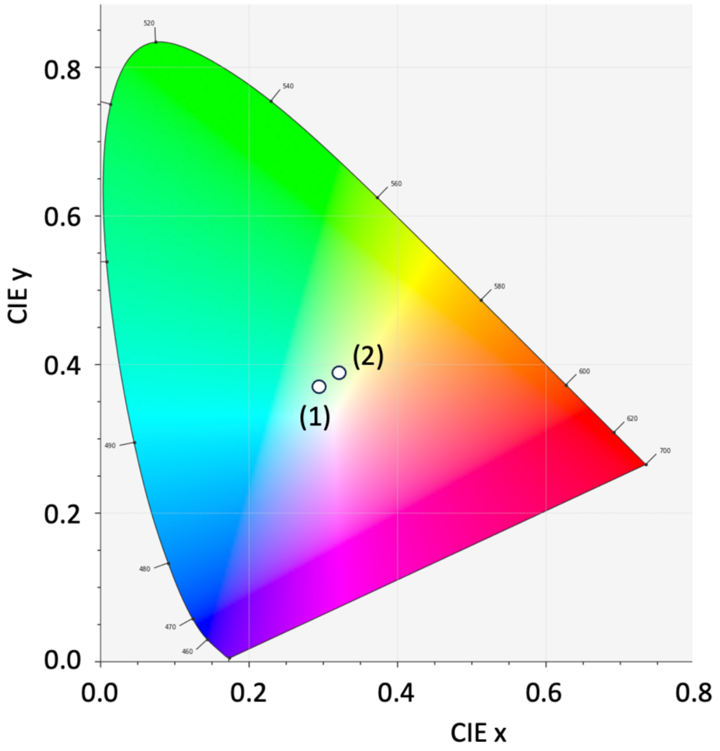

Figure S10. Chromaticity diagram where points 1 and 2 stand for CCPN-16 and CCPN-17 glazes, respectively.

❖ Density measurements of glazes

The densities of the glasses are measured using a hydrostatic balance, which measures the Archimedes's thrust. The process involves weighing a glass piece in air (m_{air}) and then the same piece, immersed in ethanol of known density, (m_{liquid}). The density is calculated using the formula:

$$\rho_{glass} = \rho_{ethanol}(T)\frac{m_{air}}{m_{air} - m_{liquid}}$$

Multiple pieces without cracks or bubbles are measured and the average values are reported in Table S3. The density of CCPN-17 is slightly underestimated due to the presence of small bubbles.

Table S3. Densities of the glazes.

	BX9	CCPN-16	CCPN-17	EPR-27ter 880 °C	EPR-27ter 1250 °C
Density ($g.cm^{-3}$)	2.56 ± 0.01	2.45 ± 0.01	2.3 ± 0.01	3.29 ± 0.01	3.24± 0.01

❖ Copper content in glasses

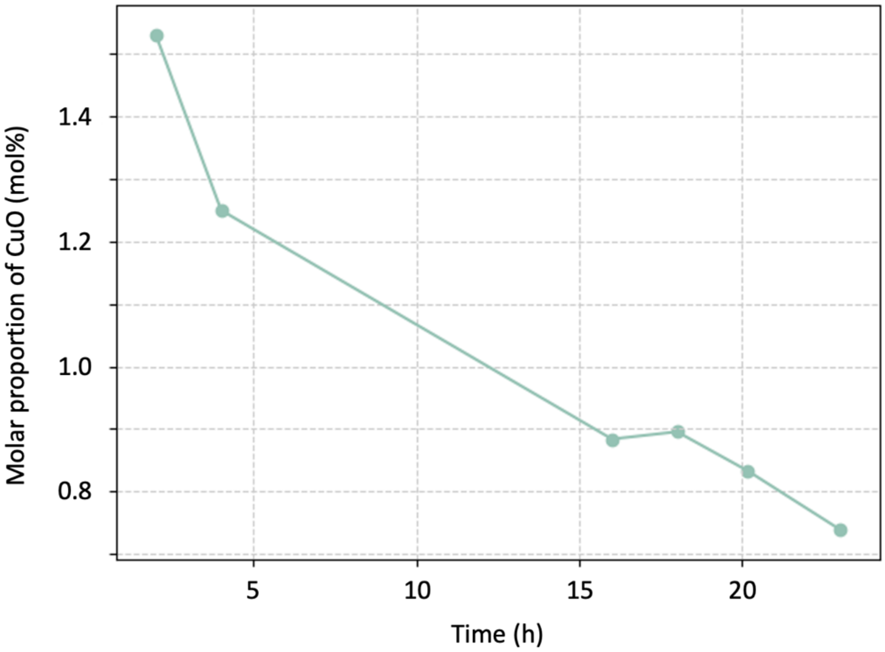

Figure S11. Proportion of copper (mol%) measured by EPMA against the melting time for CCPN-17.

Table S4. Proportion (mol%) of FeO determined through EPMA in Sevres samples.

	CCPN-16	CCPN-17	EPT-27ter 880°C	EPT-27ter 1250°C	BX9
FeO content (mol%)	0.12(4)	0.11(1)	traces	traces	0.05(4)

❖ Fit of the optical absorption spectra

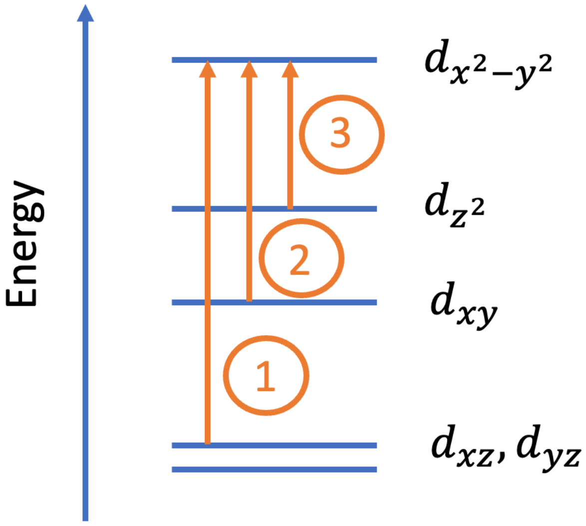

Figure S12. Number for the transitions used in the fitting of the Cu^{2+} absorption band.

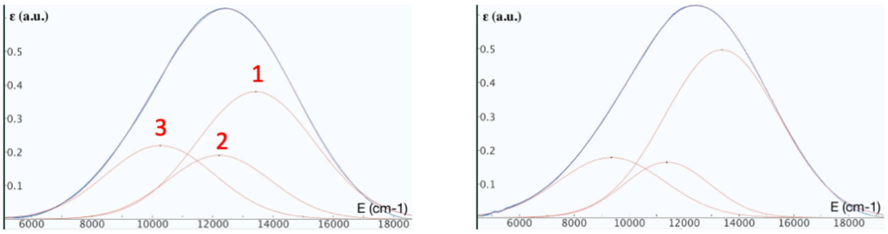

(a) CCPN-16

(b) CCPN-17

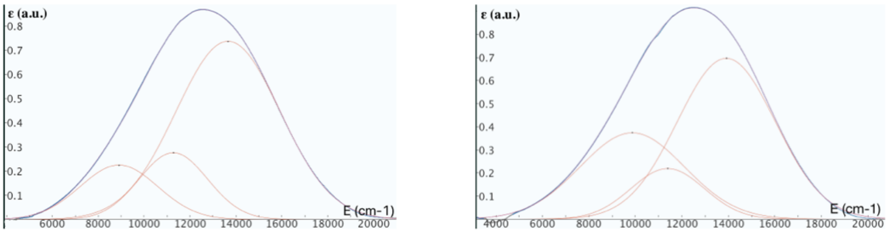

(c) EPT-27ter-880°C

(d) EPT-27ter-1250°C

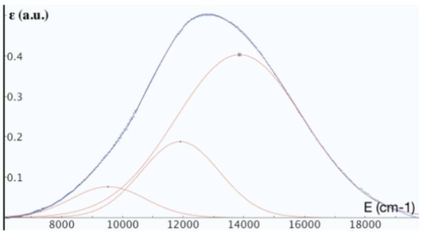

(e) BX9

Figure S13. Fit of the Cu^{2+} absorption band comparing the experimental spectra (blue curves) with the three Gaussian functions (red curves). A straight line was used for the baseline. Though not significantly changing the trend, it would be more accurate to use the tail of a Gaussian, with the maximum positioned in the UV.

❖ Fit of the EPR spectra

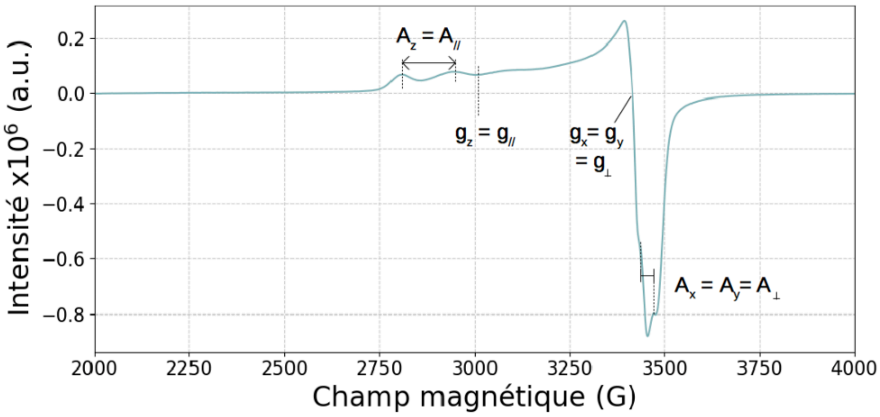

Figure S14. EPR spectrum for BX9 showing the EPR parameters in axial symmetry.

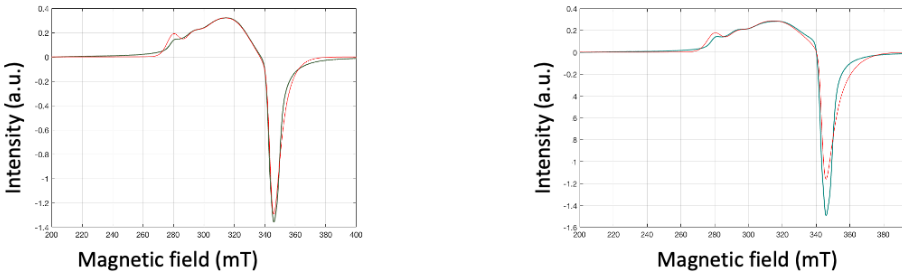

(a) CCPN-16 (b) CCPN-17

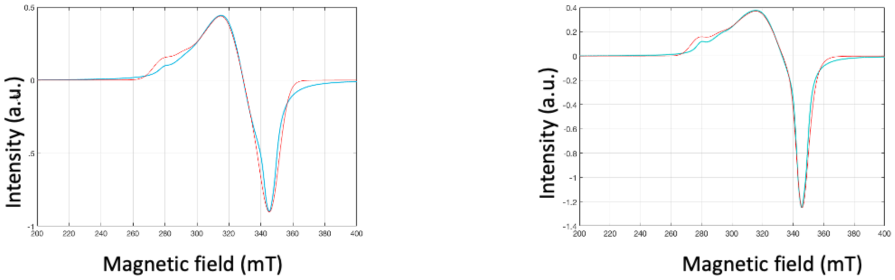

(c) EPT-27ter-880°C (d) EPT-27ter-1250°C

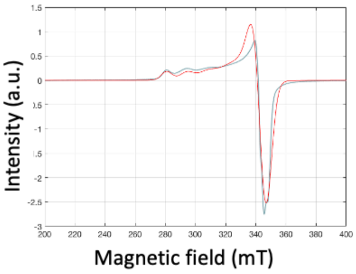

(e) BX9

Figure S15. Comparison of the experimental EPR spectra (blue curve) with the fit (red curve).

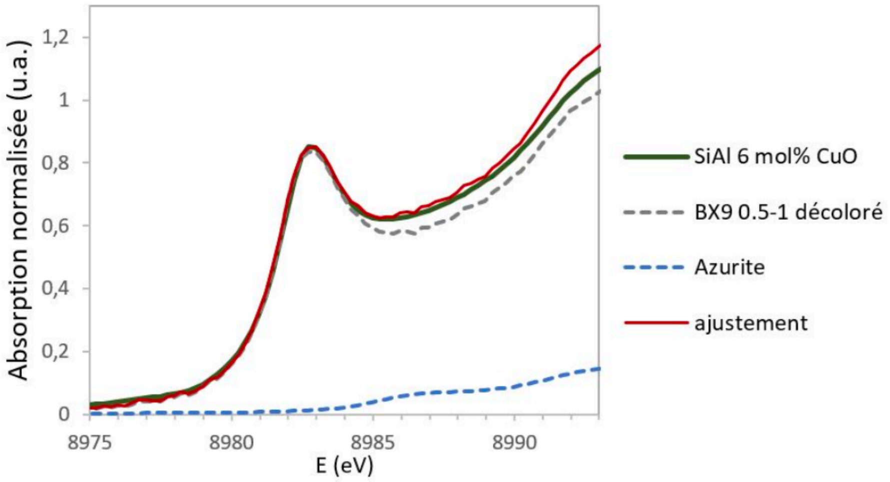

Figure S16. Example of fit of the XANES spectra at the Cu K-edge using two references: azurite, $Cu_3(OH)_2(CO_3)_2$, for Cu^{2+} and a glass of known redox for Cu^{+}.

References

d'Albis, A., 2003. Traité de la porcelaine de Sèvres. Faton, Dijon, France.

Kubelka, P., Munk, F., 1931. Ein Beitrag zur Optik der Farbanstriche. Z Techn Phys 12, 593–601.

Vercamer, V., 2016. Spectroscopic and structural properties of iron in silicate glasses (PhD Thesis). Université Pierre et Marie Curie - Paris VI, Paris.